Title

Investigation into Utrafast Dynamics of Organometallic Compounds with Transient Resonance Infrared Spectroscopy and Growing String

Author

Schlegel, Jacob Peter

Publication Date

2012

Ultrafast Dynamics of Organometallic Compounds with Transient Resonance Infrared Spectroscopy and Growing String

By

Jacob Peter Schlegel

A dissertation submitted in partial satisfaction of the

requirements for the degree of

Doctor of Philosophy

in

Chemistry

in the

Graduate Division

of the

University of California, Berkeley

Committee in charge:

Professor Charles B. Harris, Chair
Professor Graham Fleming
Professor Robert Dibble

Fall 2012

Abstract

Ultrafast Dynamics of Organometallic Compounds with Transient Resonance Infrared Spectroscopy and Growing String

by

Jacob Peter Schlegel

Doctor of Philosophy in Chemistry

University of California, Berkeley

Professor Charles B. Harris, Chair

Two systems were studied using either a pump-probe spectroscopic technique or a density functional theory computational method. Ultrafast time-resolved infrared spectroscopy has been used to investigate the reactivity of $V(CO)_5$, a doublet species, with silicon–hydrogen and carbon–hydrogen bonds. Using a ultraviolet pump pulse, a carbonyl was dissociated from $V(CO)_6$ while dissolved in triethylsilane; subsequently, a broad bandwidth infrared pulse interrogated the system. On timescales less than 1 ns, vanadium pentacarbonyl does not appear to react. The second study used the Growing String Method incorporating density functional theory to examine the possible reaction mechanisms for the fluxional rearrangement of $Fe_3(CO)_{12}$ and $Ru_3(CO)_{12}$. Fluxional mechanisms have structurally identical reactants and products; the atoms swap positions with other atoms of the same element. The concerted bridge-opening, bridge-closing mechanism for the $Fe_3(CO)_{12}$ was calculated to have the lowest barrier of those tested at 0.777 kcal/mol; in this mechanism, all twelve carbonyl change position and the final structure is equivalent to the initial structure. At 4.285 kcal/mol, the next lowest energy barrier was calculated for the Cotton's Merry-Go-Round mechanism.

To my family

Table of Contents

List of Figures

List of Tables

Acknowledgments

This work was funded by grants from the National Science Foundation, Inorganic and Physical Chemistry Divisions and the U.S. Department of Energy, Office of Basic Energy Science, Chemical Sciences Division under contract CSD DE-AC02-05CH11231 and the grant of CSR002 Directorate (Fleming) which provided specialized equipment.

I would firstly like to thank the members of the Charles Harris Group for providing a fun and intellectually stimulating environment to perform, and not to perform, research: Charles for creating a unique self-perpetuating group; Vijaya Narasimhan for keeping us in the green even when we did not realize it; Matthias Kling, Libby Glascoe, and Jennifer Shanoski for showing how the work is done; members of the surface side for providing both the brains and the wacky entertainment of the group; and my classmates, Karma Sawyer and James Cahoon, for support and hard work during those trying times. It was also a privilege to work next to Matthew Zoerb and Eric Muller as they progressed from their first year as graduate students.

Prof. Dick Andersen and Marc Walter both deserve thanks for helping synthesize what may be the last vanadium hexacarbonyl to ever exist on planet Earth–the former especially for an interesting insight into radical chemistry. Prof. Martin Head-Gordon and Rob DiStasio, Jr. deserve more than thanks for essentially providing the platform for my fluxionality project.

Lastly, I wish to thank my family and the Rt. Rev. Caleb for emotional support for all these years.

1 Introduction

> How far is far? How small is small? How much greater than is "much greater than?" [*sic*] Obviously the questions cannot be answered with any precision except in reference to an experiment which may not exist. Although we shall not attempt to emphasize their occurrence, there are a number of articles wherein "much greater than" really amounts to "equal to." It does seem proper, however, that such restrictions are often rendered almost meaningless in application.
>
> —R. G. Breene, Jr. *Theories of Spectral Line Shape* [1]

A complete understanding the nature of a chemical reaction involves not only characterizing the reactants and products and their rate of conversion but also examination of the structure of the reactants that lead to the reaction and the identity of all intermediate forms. The goal of this work is to describe certain reactions using ultrafast time-resolved UV-pumped IR-probed spectroscopy and computational methods that involve density functional theory. Pump–probe spectroscopy and density functional theory have decades of success in elucidating the dynamics of chemical reactions [2-13]. These techniques are applied separately here to the study of two classes of chemical reaction.

While both chemical reactions involve organometallic compounds, the first belongs to the class of initiated reaction between the molecule of interest and the solvent. Past work had shown a difference in reactivity dependent on the number of unpaired electrons in the organometallic complex (either zero or two unpaired electrons) [12, 14] and inspired the study presented here where a complex with only one unpaired electron was generated and left to react (or not as the case here) with the solvent (Chapter 3). The second reaction belongs to thermal rearrangements of the organometallic complex called "fluxions." There a molecule gains enough energy from the bath to rearrange its geometry, ending with the same structure except that atoms of the same element have exchanged position [15]. This work had been motivated by the work of Cahoon et al. that validated the Berry pseudorotation in $Fe(CO)_5$, but examined a more complex molecule whose fluxional mechanism has also been debated in the literature [16-25]. While examination of the fluxional mechanism by two-dimensional infrared spectroscopy proved untenable due to spectral congestion and low solubility, the use of the Growing String Method produced results by modeling the reaction with density functional theory computational methods (Chapter 4) [26] [27].

1.1 Molecular Dynamics

The work detailed here pulls from two distinct classes of reaction. The first class is the thermal reaction. For this class, the reactant is capable of passing up and over the barrier using only thermal energy (see Figure 1.1). The second class is the photochemically activated reaction. They require a photon of certain energy to promote the reactant into another electronic state whereupon the reaction proceeds (see Figure 1.2).

1.1.1 Thermal reactions

For thermal reactions to proceed, the reactant molecules must have enough internal energy to cross the transition state barrier and form the product molecules. This internal energy includes sensible heat which is related to the temperature of the system. The sensible heat is associated with the kinetic energy, which itself includes translational, rotational and vibrational energy. Within a system at equilibrium, the molecules possess an internal energy that exists within a statistical distribution [28].

Initially, not all reactant molecules may have enough internal energy for the reaction to proceed. At low temperatures, the vast majority of molecules do not possess enough energy to reach the transition state (TS). As the temperature increases, the average energy of the molecules increases along with the number of high-energy molecules, molecules with enough energy to surmount the barrier.

Once the reactant reaches the TS, it can immediately fall down the potential energy surface toward the product. Because of this and the statistical nature of barrier crossing, very few molecules will exist at the TS at a single instant. The ephemeral nature of the transition state complicates its study [29]. At the same time, the transition state of the thermal reaction demands study as its very nature governs the entire chemical reaction. The work presented in Chapter 4 aims to characterize the transition states of a set of transition-metal–carbonyl clusters.

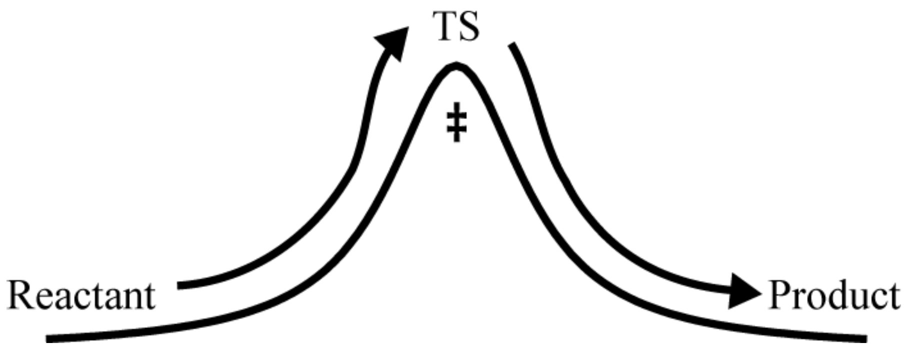

Figure 1.1 Thermal Reaction
A reaction coordinate for a thermally activated reaction where the reactant and product are isoenergetic. TS and the double dagger mark the transition state.

1.1.2 Photochemical reactions

Photochemical reactions gain the energy to react from an absorbed photon [30]. Generally, this photon excites the molecule from the ground electronic state to an excited electronic state (see Figure 1.2), leading eventually to conversion to another species or return to the ground state. In between the excitation and the final result, the molecule relaxes by falling along a series of intermediary states. If there is a barrier between intermediary states, then the lifetime of the former state may be long enough to permit characterization. All excited states can be classified as bound (nondissociative) or repulsive (dissociative), though a molecule may pass from one to the other as it relaxes [31].

In a bound excited state, as is the case for metal-to-ligand charge transfer (MLCT) states, the molecule seeks to accommodate change in charge distribution by altering its geometry. This, then, results in a solvent rearrangement for condensed-phase reactions. For dissociative states, at least one chemical bond is broken. A new structure is then formed from internal rearrangement or by coordination of another molecule. When this coordination is weak and does not lead to bond formation, the dissociated species is said to be solvated. This feature is especially important for the work presented in Chapter 3.

Transition-metal–carbonyls are of particular interest for work within the Harris group[2, 6, 8, 10-14, 32-43]. As such a brief discussion of their photochemistry is presented. Upon absorption of a UV photon (266 nm, in this work), the molecule is excited into a ligand field state where electron density has been transferred into a manifold of the π^* orbitals of the carbonyls. As the molecule relaxes, it travels along a series of bound or repulsive states before reaching the final repulsive state, all in less than 100 fs. The final repulsive state has a negative slope in the direction of the lengthening of a M–CO bond, and the photodissociation reaction terminates with a coordinatively unsaturated transition-metal–carbonyl species and a carbon monoxide molecule. This series of events contrasts with the results of a lower energy excitation (such as with a 400-nm photon). Although energetic enough to dissociate a M–CO bond, the visible photon does not generally cause a dissociative event. Instead the molecule, if it does absorb in this region of the spectrum, likely experiences a MLCT that causes a geometric shift, such as bond lengthening or a linearly bound nitrosyl bending, before returning to the ground state geometry. An exception is molecules with M–M bonds which are broken by visible excitation [44].

Whether coordinatively unsaturated or structurally unstable, these species represent a class of transient intermediates that can, in the presence of a coreactant or on a longer timescale, go on to form new species. The study of these transients informs on the overall reaction mechanism. When understood fully, the reaction mechanism provides both a deeper understanding of chemical dynamics and reactivity and the possibility of improving synthetic methods.

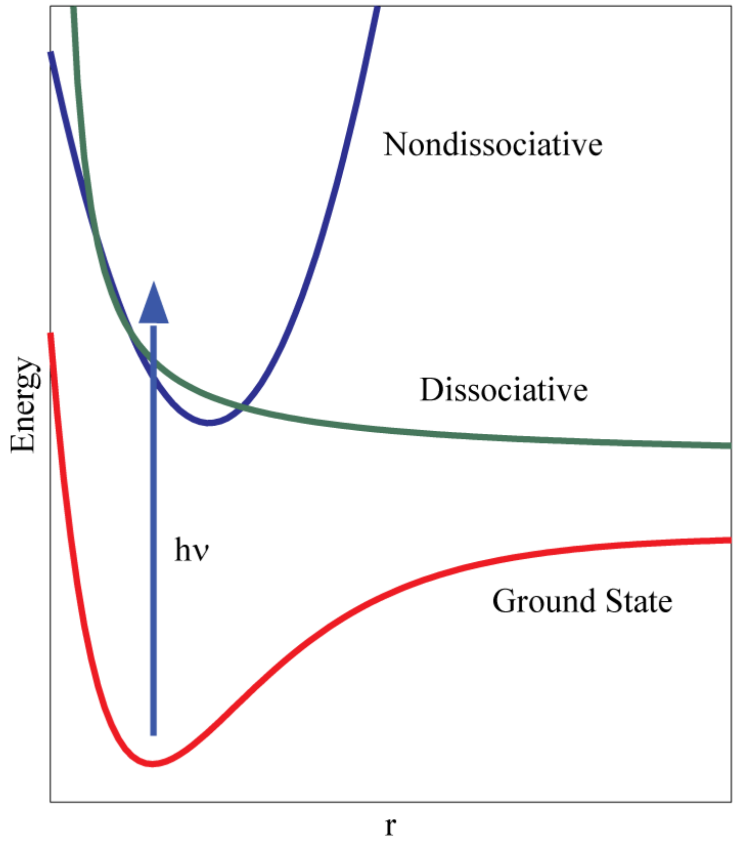

Figure 1.2 Photochemical Reaction
A set of potential energy curves for a reaction that is activated by a photon of energy hν. The molecule is excited to either a dissociative (green) or nondissociative (blue) curve with the possibility of curve crossing.

1.2 Spectroscopic Methods

Pump-probe spectroscopy encompasses an array of techniques that feature an initial excitation followed in time by an interrogation. It is particularly useful for studying the transient species in chemical reactions [7, 12, 45-47]. Both of the techniques presented here fall under ultrafast pump-probe vibrational spectroscopy as they employ an infrared probe pulse. The first technique is time-resolve infrared spectroscopy (TRIR), which uses an UV pump pulse; and the second is two-dimensional infrared spectroscopy (2DIR), which uses an infrared pump pulse. Both pulse sequences are shown in Figure 1.3. By scanning the delay between pump and probe, one can monitor the progress of the reaction. The experimental apparatus is described in Chapter 2.

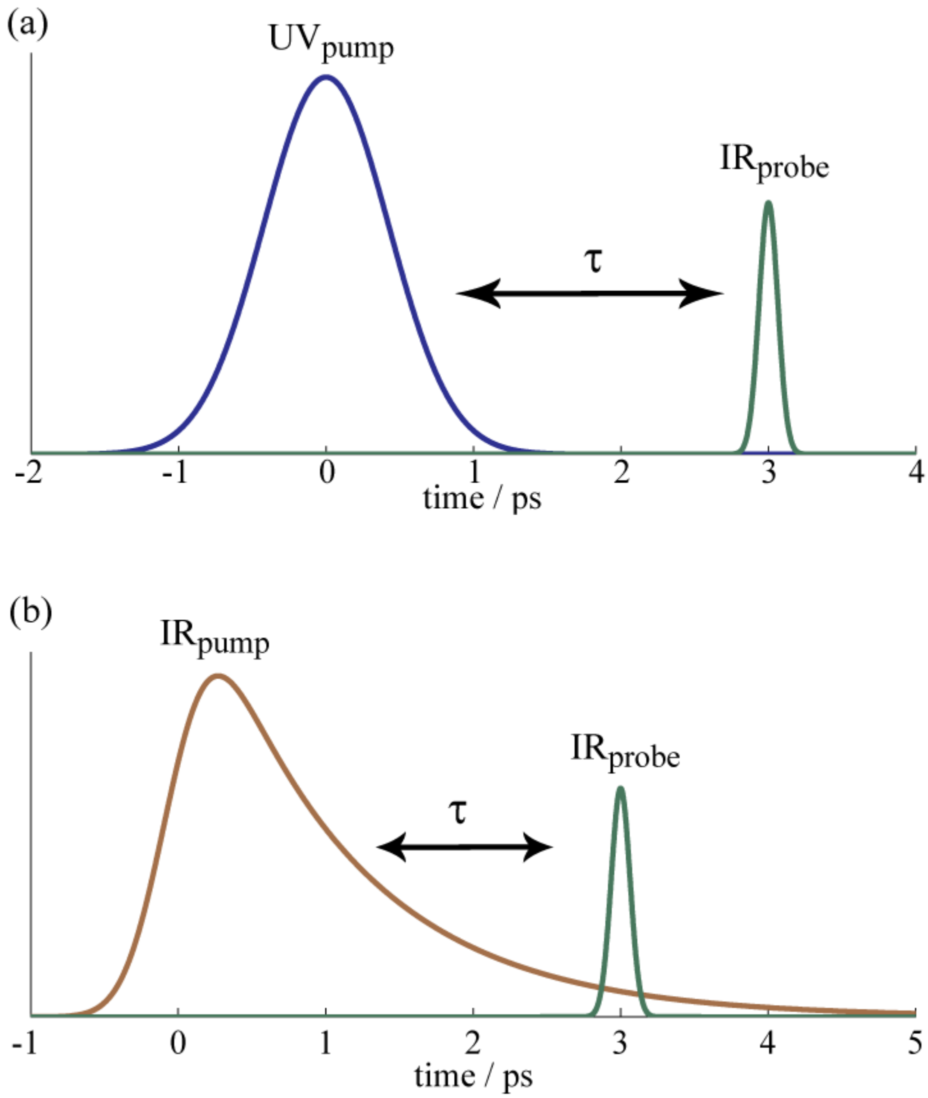

Figure 1.3 Pulse Sequences
Pulse sequences for (a) time-resolved IR spectroscopic experiments and (b) two-dimensional IR spectroscopic experiments.

1.2.1 The probe ligand

In the spectroscopic methods used for these studies, characterization of the molecular system is reliant on absorption of infrared light by carbonyl (CO) ligands. Carbonyl ligand are an excellent probe as they have a strong, sharp absorption and are sensitive to changes in electron density on the metal center [48]. Figure 1.2 shows the nature of the bonding between a carbonyl and a metal atom which is key to its sensitivity. In addition to the σ interaction, there is donation of electron density back to the carbonyl's π* orbitals through a π bond. Any additional electron density in the carbonyl's π* orbitals causes a weakening of the C–O bond. The strength of the C–O bond is related to the frequency (ω) of the vibration of that bond through

$$\omega = \sqrt{\frac{k}{\mu}}$$

where k is the force constant of the bond and μ is the reduced mass of the two bound atoms. During a chemical reaction, the electron density in the metal complex alters the level of back-donation to the carbonyl and, consequently, its vibrational frequency.

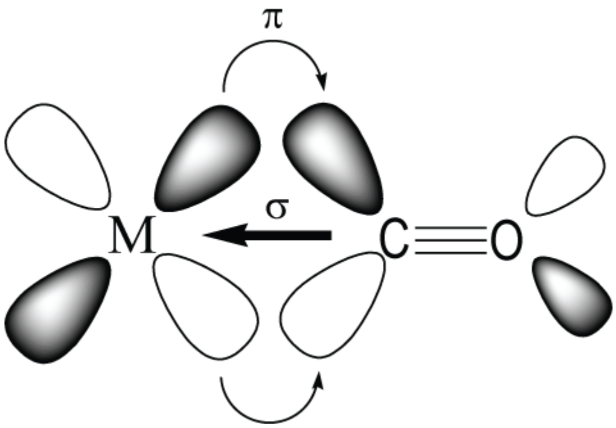

Figure 1.4 Metal–Carbonyl Bonding
A transition metal forms σ bonds with a carbonyl ligand and back-donates electron density through π interactions into the π* molecular orbitals of the carbonyl.

In addition to a linear orientation, where ∠MCO ≈ 180°, the carbonyl ligand is capable of bonding simultaneously to two metal atoms in a bridging geometry. The stretching vibration of a bridging carbonyl is typically 1750–1850 cm^{-1}, which is lower than the 1850–2125 cm^{-1} stretch of the linearly bonded, or terminal, carbonyl [44].

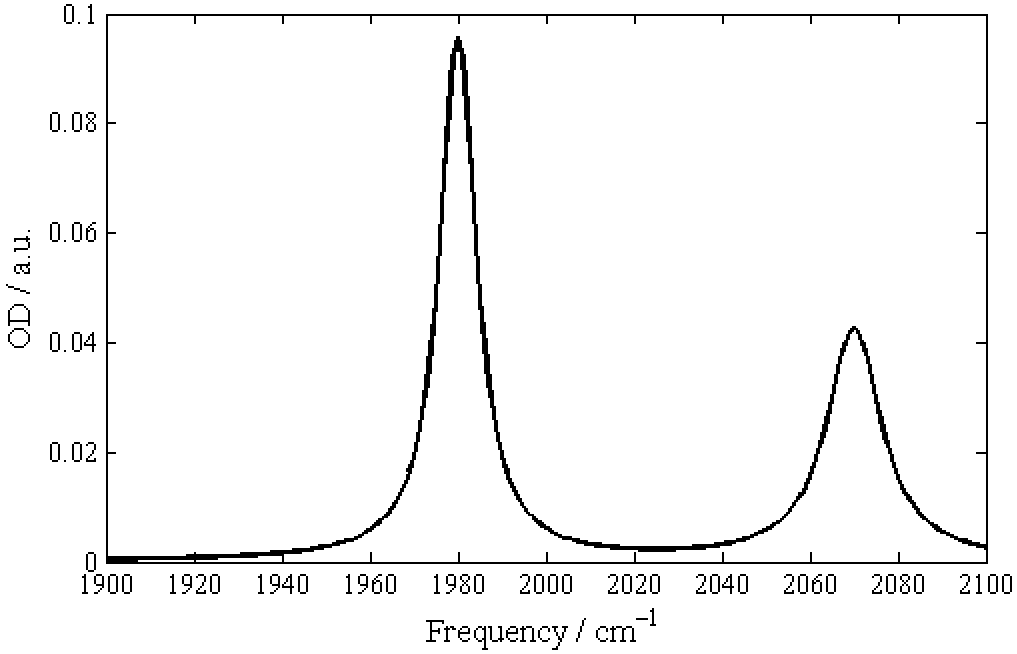

Figure 1.5 Illustrative IR Absorption Spectrum

1.2.2 UV-pump, IR-probe spectroscopy

In a linear IR absorption spectrum, a peak or set of peaks indicate the presence of a species whose vibrational frequency matches that of the IR light being absorbed. Figure 1.5 is an illustration of the static IR spectrum of a species with two distinct carbonyl stretching modes. As discussed above, carbonyl ligands are excellent indicators of the condition and identity of the compound when probed with IR light in the range 1700–2125 cm^{-1}. When this species is first excited by a UV pump, the IR absorption spectrum will show initially, at least, a number of differences with the static spectrum. The first being the peak areas at 1980 and 2070 cm^{-1} will decrease due to depletion of the so-called "parent" species—the compound initially present. The second change is the appearance of new peaks belonging to intermediate or product species. For this illustration, new peaks appear at 1930 and 2020 cm^{-1}. To present clearly this data, spectroscopists commonly choose the format of the difference spectrum where the absorption spectrum of the pumped species (A_{pumped}) is subtracted from the static spectrum ($A_{unpumped}$) as

$$\Delta A = A_{pumped} - A_{unpumped} = -\log\left(\frac{I_{pumped}}{I_0}\right) + \log\left(\frac{I_{unpumped}}{I_0}\right),$$

where ΔA is the difference spectrum, I_0 is the reference beam intensity, and I_{pumped} and $I_{unpumped}$ are the IR intensities when the UV pump is on and off, respectively. The difference spectrum for this example is shown in Figure 1.6. One notices that the parent peaks have negative intensity—they are therefore called “bleaches”—and the intermediate or product peaks have positive intensity. The probe pulse covers an approximately 200-cm^{-1} range at one time; this is a broad enough spectral region to cover all carbonyl stretches for a typical system.

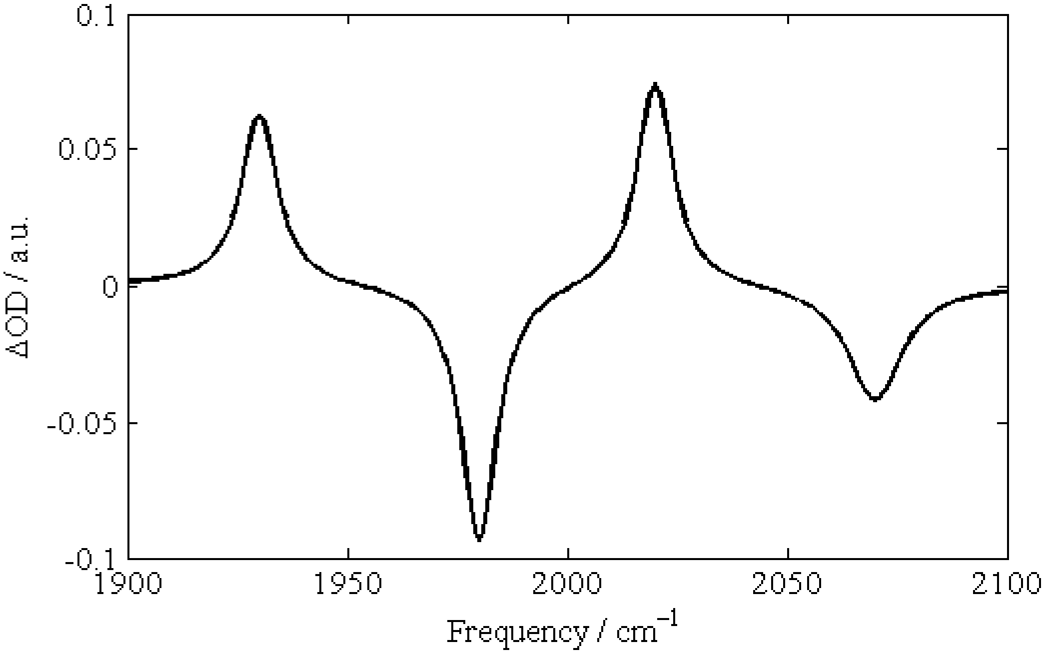

Figure 1.6 Schematic TRIR Spectrum

1.2.3 Two-dimensional IR spectroscopy

While it excels at monitoring photoinitiated chemical reactions, TRIR cannot be used to study systems at equilibrium or thermally driven reactions; the UV/Vis pump pulse is too great of a perturbation to the system. If, on the other hand, one tags a specific vibration with an IR pump pulse, the system remains in the initial electronic state, and the probe pulse interrogates a quasi-equilibrium system. The IR-pump, IR-probe pulse sequence is the essence of 2DIR spectroscopy.

Over the past decade, a number of research groups have advanced the 2DIR [46, 49-64] spectroscopic technique and the corresponding theory, which is behind the data analysis. The systems studied range from liquid water to inorganic species to complex proteins, and the results have provided valuable information.

The Harris group chose to incorporate the 2DIR spectroscopic technique into our study of organometallic reaction dynamics, and our first task was elucidating of the long-debated mechanism for fluxionality in $Fe(CO)_5$. With a transition state in mind, one can map the vibrational modes from the initial geometry onto the modes at the transition state then onto the modes of the final geometry (Figure 1.7). This approximates the energy splitting from an IR-pump, IR-probe spectroscopic experiment; the results can be modeled using structures derived from computational studies.

This method is briefly remarked on due to its relevance for fluxionality studies, but use of this method did not provide results for these particular studies as will be explained in Chapter 4.

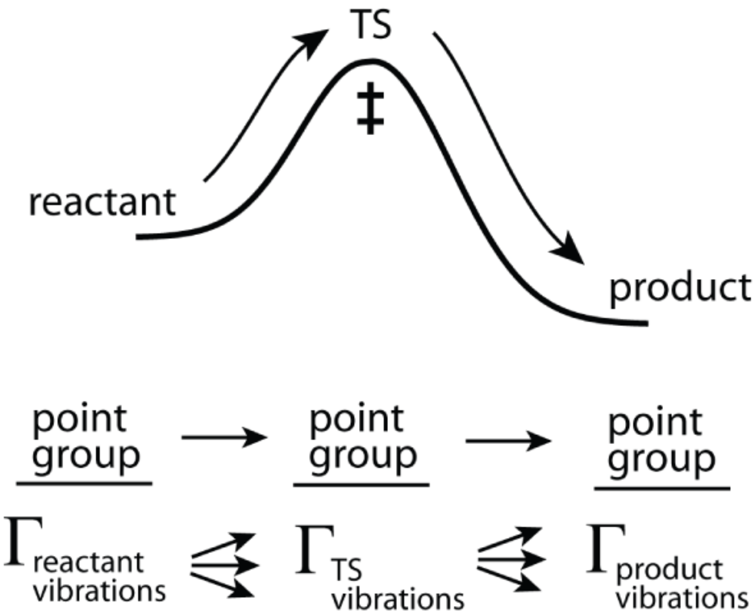

Figure 1.7 Mode-splitting
Illustration of how energy in the reactant vibrational modes redistributes as the reaction proceeds through a transition state to the product.

1.3 Theoretical Methods

For the work in Chapters 3 and 4, calculations using density functional theory (DFT) were performed. DFT calculations are known to provide reliable energies, structures, and frequencies for transition-metal complexes in both the ground and the transition state. The computational methods for the work in Chapter 4 were used to optimize molecular structures, find relative thermodynamic information, and calculate vibrational frequencies of both ground and transition state geometries. With these results, we were able to identify vibrational modes in the IR spectra, calculate barrier heights and reaction rates, and, eventually, identify reaction mechanisms. The details of the DFT methods used are presented in the corresponding chapter.

1.3.1 Growing String Method

Growing String Method (GSM) is an interpolation algorithm for finding the minimum energy pathway and transition state for a given reaction [26, 27, 65-67]. It was devised in response to the perceived flaw of both the nudged elastic band and string method, the flaw being that they require the user to input a good initial guess for the reaction pathway. GSM requires only the reactant and product configuration from the user.

Figure 1.8 is a schematic example of the GSM process. The six graphs are the same potential energy diagram of a basic reaction, R→P, whose transition state is marked with a double dagger. After calculating the relative energies of the user-input reactant and product geometries, GSM initiates two nodes along a linear synchronous transit path connecting R and P (cell B). The geometry of each node is then optimized to minimize force orthogonal to the reaction coordinate (cell C). As the position of the nodes in coordinate space is optimized, more nodes are added (along a cubic spline) and their structure optimized (cells D and E). Eventually, a string of equally spaced nodes lies along the minimum energy pathway (cell F), where the highest energy node approximates the transition state structure. At this point, the highest energy node can be further optimized using the quantum mechanical code.

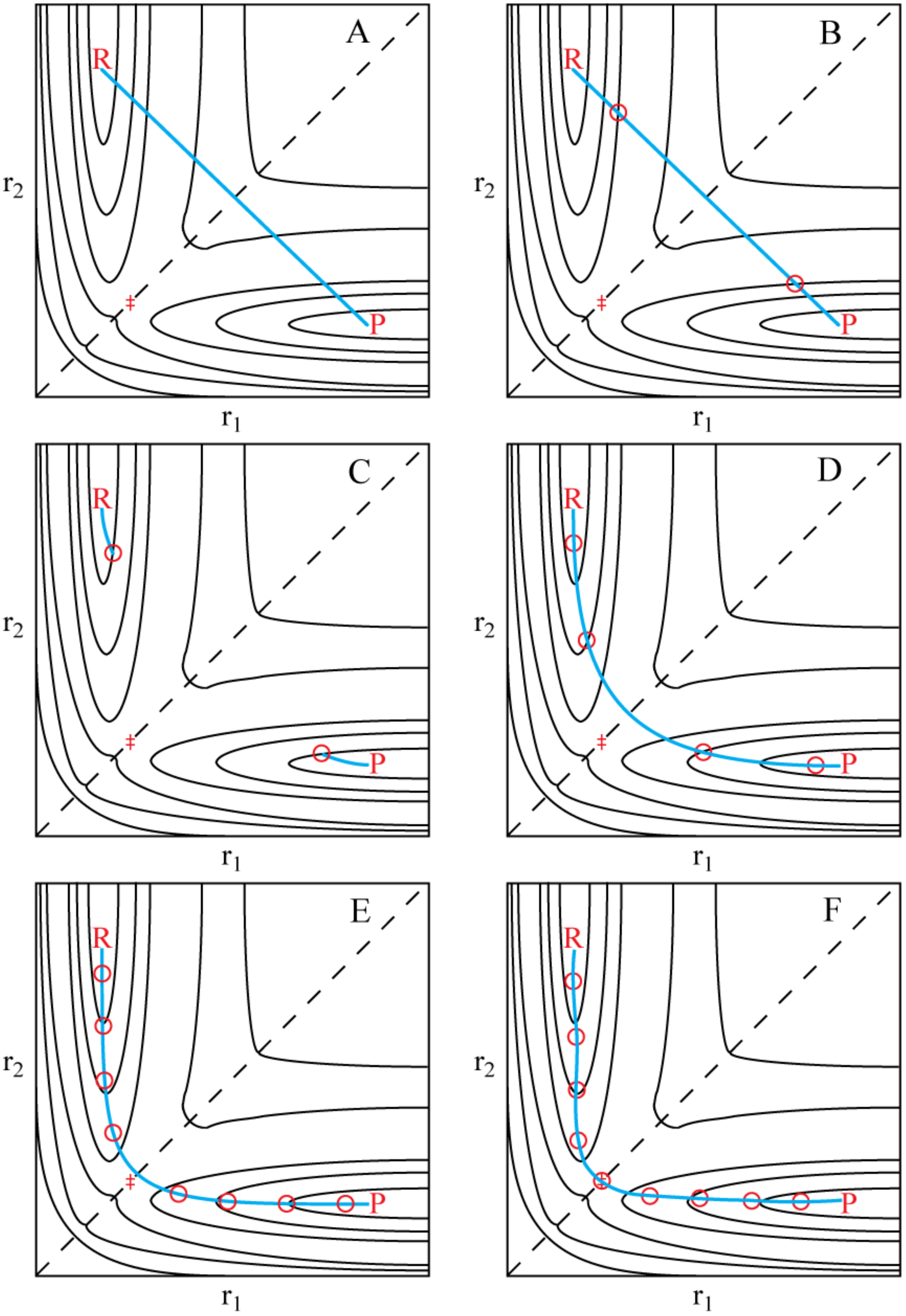

Figure 1.8 Growing String Method Diagram
See Section 1.3.1 for a description of this diagram.

2 Methods

2.1 Ultrafast Laser Techniques

The two spectroscopic experiments presented here are Time-resolved Infrared Spectroscopy (TRIR) and Two-dimensional Infrared Spectroscopy (2DIR). The former, sometimes referred to as One-dimensional Infrared Spectroscopy (1D-IR), requires two precisely timed laser pulses, one an ultraviolet or visible pulse and the other a broad-bandwidth infrared pulse. The latter requires two precisely timed laser pulses, one a narrow-bandwidth infrared pulse and the other a broad-bandwidth infrared pulse. In either experiment, the first pulse is used to pump the sample to an excited state (electronic or vibrational, respectively) while the second pulse probes the state of the system. As such, both experiments fall into the pump-probe method of spectroscopy.

In the past several years, the design of the experimental setup has gone through a number of variations and upgrades [54]. Where appropriate, an asterisk marks an aspect of the older setup specific to work in Chapter 3. Otherwise the latest design is presented in Figure 2.1.

Component Label	Description	Manufacturer
Nd:YLF	Q-switched, diode-pumped 1 kHz, 15 W, 532 nm	Spectra-Physics Empower-15
Nd:YLF*	Q-switched, diode-pumped 1 kHz, 10 W, 532 nm	Spectra-Physics Evolution-X
Nd:YVO4	CW, diode-pumped 5W, 527 nm	Spectra-Physics Millenia-VsJ
Oscillator	80 MHz, 650 mW, 80 fs, 800 nm (FWHM=13 nm)	Spectra-Physics Tsunami
Regenerative Amplifier	1 kHz, 0.9–1.4 W, 90 fs, 800 nm	Spectra-Physics Spitfire

Table 2.1 Commercial laser system components
Refer to Figure 2.1 for placement in the laser setup.

2.1.1 Generation of ultrashort laser pulses

Ultrashort laser pulses are used to give both the time resolution and frequency bandwidth needed for the spectroscopic experiment presented here. We use a commercial laser system to produce ~90-fs laser pulses centered at 800 nm. This commercial system comprises a 5-W, diode-pumped Nd:YVO$_4$ continuous-wave laser (Spectra-Physics, Millenia Vs); an 80-MHz Ti:sapphire oscillator (Spectra-Physics, Tsunami); a 1-kHz, 15-W [10-W]*, Q-switched and diode-pumped Nd:YLF laser (Spectra-Physics Empower-15 [Spectra-Physics Evolution-X]*); and a Ti:sapphire regenerative amplifier (Spectra-Physics, Spitfire). The Nd:YVO$_4$ laser pumps the oscillator which seeds the amplifier which is pumped by the Nd:YLF laser. The output of the amplifier is a 1-kHz pulse train and has a power up to 1.4 W.

The output of the commercial system is split, to varying degrees, between generation of infrared light by one or two optical parametric amplifiers and generation of UV/visible light by harmonic generation or a non-collinear optical parametric amplifier.

Component Label	Description	Manufacturer
AGS	$AgGaS_2$ crystal $5x5x1.5mm^3$, θ=34.1°, ϕ=45°	Red Optronics
BBO1	Type 1 BBO crystal $5x5x0.7mm^3$, θ =29.2°, ϕ=0° p-coated @ 800 nm	Photox Optical Systems
BBO2	Type 1 BBO crystal $5x5x1mm^3$, θ =33°, ϕ=90° p-coated @ 400 nm	Photox Optical Systems
BBO3	Type 1 BBO crystal $5x5x2mm^3$, θ =33°, ϕ=90° p-coated @ 400 nm	Photox Optical Systems
BBO4	Type 1 BBO crystal $6x6x0.2mm^3$, θ =44.3°, ϕ=0° p-coated @ 400 nm	Red Optronics
BBO5	Type II BBO crystal $4x4x4mm^3$, θ =28.9°, ϕ=30° p-coated @ 800 nm	Photox Optical Systems
BBO6	Type II BBO crystal $4x4x4mm^3$, θ =28.9°, ϕ=30° p-coated at 800 nm	Red Optronics

Table 2.2 Nonlinear crystal components
Refer to Figures 2.2 and 2.3 for placement in the laser setup.

2.1.2 Generation of ultraviolet and visible light*

For TRIR experiments, part of the output from the regenerative amplifier is used to generate ultraviolet or visible light (see Figure 2.2). Light from the regenerative amplifier is split such that 30–40% is directed first through a telescope, delay line (see Section 2.1.4), and periscope before arriving at the harmonic generator or non-collinear optical parametric amplifier (NOPA). For experiments requiring higher energy pump photons, ultraviolet light is created by third harmonic generation from 800-nm light. For experiments that require lower energy pump photons, visible light is created in one of two ways: second harmonic generation from 800-nm light or non-collinear optical parametric amplification. This portion of the apparatus has been well described in the dissertation of Dr. Elizabeth Glascoe [68].

Harmonic generation of 266- and 400-nm light is accomplished by sum frequency generation (SFG) in a β-barium borate crystal (BBO). SFG is a well understood nonlinear optical process that is well described elsewhere. When the induced polarization of a medium is expanded in a power series, the second-order polarization $P^{(2)}$ is defined as

$$P^{(2)}(t) = 2\chi^{(2)}(\omega_1 + \omega_2, \omega_1, \omega_2)E(\omega_1)E(\omega_2)e^{-i(\omega_1+\omega_2)t},$$

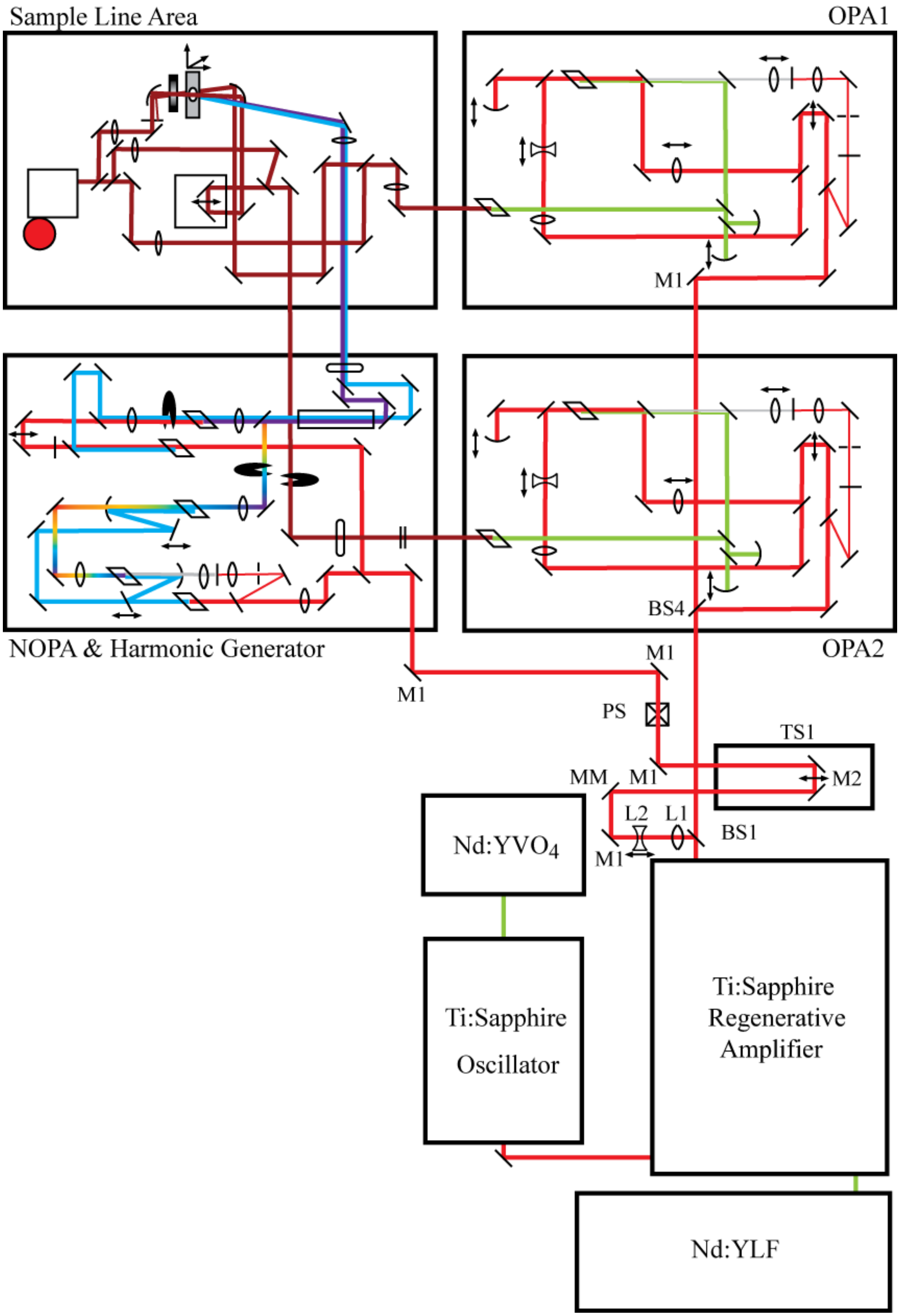

Figure 2.1 Laser system diagram

For details on components, refer to Figures 2.2–2.4 and Tables 2.1–2.5.

where $\chi^{(2)}$ is the second-order nonlinear susceptibility of the medium, and $E(\omega_1)$ and $E(\omega_2)$ are the incident electric fields. Here, the 800-nm light is focused onto BBO1 to create 400-nm light. Here the 400-nm light corresponds to $\omega_1 + \omega_2$ in the above equation. The residual 800-nm light is separated, has its polarization rotated 90° by a half-wave plate (WP1), and is recombined with the 400-nm light before passing through BBO2 to create 266-nm light. Here 266-nm light corresponds to $\omega_1 + \omega_2$ in the above equation. The light pulses then pass through a 250-mm-long fused silica rod, which temporally stretches the pulse to approximately 1-ps duration. The stretched pulses are separated according to wavelength, and the residual 800-nm light is discarded. Either the 266- or 400-nm light then passes through a wave plate (WP2 or WP3, respectively) mounted on a computerized rotation stage (Newport, RGV100).

The NOPA generates tunable visible light (450–750 nm). It was built by Elizabeth Glascoe and this author based on a design by Eberhard Riedle. The theory for a visible NOPA is detailed by Krylov et al. and is not summarized here.

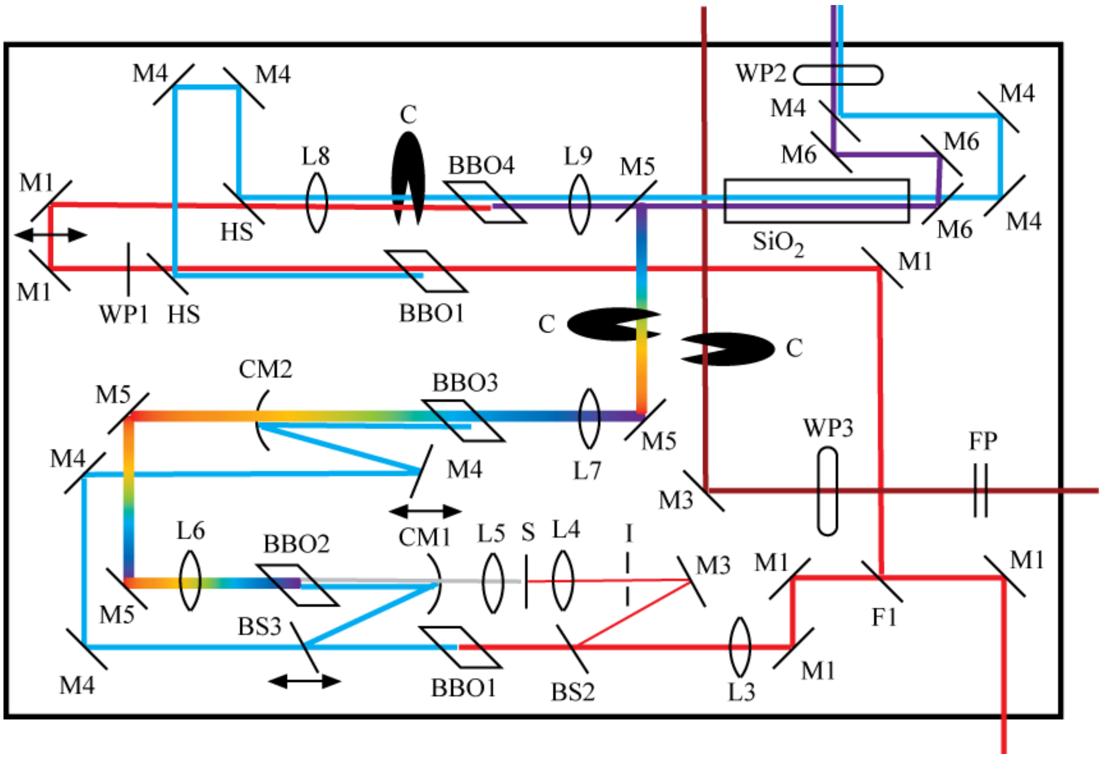

Figure 2.2 NOPA and harmonic generation diagram
For details on the optical components labeled, refer to Tables 2.2–2.5. Beam colors: 800 nm (red), 400 nm (cyan), white light (grey), tunable visible (rainbow), 266 nm (purple), and mid-IR (brown).

2.1.3 Generation of mid-infrared light

The OPA design has been described in the dissertation of Dr. Jennifer Shanoski [69]. For TRIR experiments, one broad-bandwidth mid-infrared light pulse is required, and it is generated by OPA1; in which case, BS4 at OPA2 is removed so that no mid-IR light is being produced by OPA2. For 2DIR experiments, one narrow-bandwidth and one broad-bandwidth mid-infrared light pulse are required. These two pulses are either generated together by a single OPA or generated separately by two OPAs. In the former case the output of OPA1 is split, such that 70% passes through a Fabry-Perot interferometer to create a narrow-bandwidth pump pulse and 30% becomes the signal (probe) and reference beams (see Section 2.1.4). In the latter case, the entire output of OPA1 becomes the signal (probe) and reference beams, and the entire output of OPA2 passes through a Fabry-Perot interferometer to create a tunable narrow-bandwidth pump pulse. With two OPAs, the center frequencies of the pump pulse range and the probe pulse can be varied independently for Two-color Two-dimensional IR Spectroscopy (2C-2DIR). The OPA design (refer to Figure 2.3) has been described elsewhere and is based on the design by Peter Hamm [70]. This particular design is capable of suppressing the 2–3% noise of the commercial system to levels below 1% in the mid-infrared.

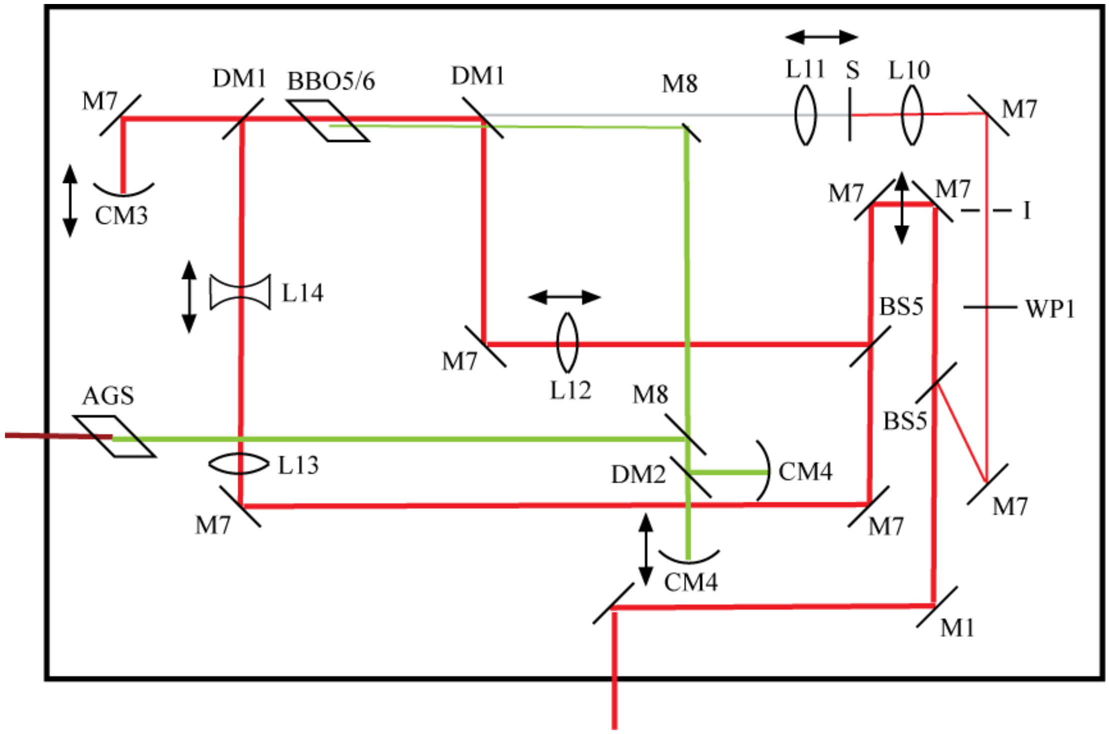

Figure 2.3 OPA diagram

For details on the optical components labeled, refer to Tables 2.2–2.5. Beam colors: 800 nm (red), white light (grey), near-IR (green), mid-IR (brown).

The 800-nm light is first split in the OPAs to create white light, a first-pass pump line, and a second-pass pump line. In BBO5/BBO6, the first-pass pump is mixed with white light (the “seed”) to create the signal and idler beams (1.2–1.7 and 1.7–2.2 μm, respectively) by optical parametric amplification. The signal is directed back through BBO5/BBO6, along with the second-pass pump, to be amplified. More idler is also created during this second pass. The signal and idler then pass together through a silver thiogallate crystal (AGS) to create tunable mid-IR light (1700–2100 cm^{-1}) by difference frequency generation. Refer to the Ph.D. dissertations of Jennifer Shanoski and Karma R. Sawyer for details on the design and optical components. Refer to the Ph.D. dissertation of James F. Cahoon for details on the Fabry-Perot interferometer with the exception of the improved design of partial reflectors therein (RMI, smooth reflectance curve of R = 82–88% over wavelength ranges of 4.7–5.3 or 5–5.6 μm).

2.1.4 Timing pulses, polarization control, and the sample line area

Both TRIR and 2DIR experiments require precise control over the time delay between the pump pulse and the probe pulse. This is achieved by directing each pump line through a delay line comprising a set of mirrors atop a computerized translation stage. For the TRIR experiment, 30–40% of the 800-nm beam is directed through a 3:1 reducing telescope and into a single-pass delay line by a computer-controlled mirror (MM). The delay line sets atop the translation stage TS1. For alignment, a custom LabView program controls the CCM, TS1, and a position detector (New Focus, Quadrant Photoreceiver Model 2921) placed far downstream. In upgrading TS1, we found that the laser table did not meet certain flatness criteria. Consequently, we acquired a custom-made granite base (Newport) with flatness of <2 μm. The granite base is not shown in Figure 2.1. Following the delay line, the beam is periscoped to the necessary height before entering the NOPA or harmonic generator. Between UV/visible pump generation and the sample line area, the pump beam passes through a wavelength-appropriate half-wave plate (WP2) mounted on a computer-controlled rotation stage (Newport, RGV100). The polarization of the pump beam is then held at the magic angle (54.7°) relative to the IR probe beam. Though not used in such a way in this work, WP2 can also control the UV/visible polarization for Transient 2DIR experiments which involve both UV/visible and narrow-bandwidth pump pulses.

For the 2DIR experiments, the portion of the mid-IR beam that becomes the pump pulse is directed through a Fabry-Perot interferometer and a wave plate (WP3) mounted on a computerized rotation stage (Newport, RGV100). The polarization of this IR pump beam is held at the magic angle (54.7°) relative to the IR probe beam. Following the wave plate, the pump beam is directed into a single-pass delay line. The delay line sits atop the translation stage TS2. Alignment is performed manually.

In the sample area (refer to Figure 2.4), the pump beam (either UV/visible or IR narrow-bandwidth) and the signal beam are directed in parallel onto a off-axis parabolic mirror (PM) that focuses the beams onto a single point at the sample. After passing through the sample, the beams first pass through a wire-grid polarizer (WG) to eliminate scattered pump light from the signal beam then are recollimated by another off-axis parabolic mirror. The signal beam is then directed into the spectrograph (SG). Along a side path, the reference beam is sent directly to the spectrograph. For characterization the pump beam can be directed by a computer-controlled flipper mirror (F2) directly into the spectrograph.

The sample cell (Harrick Scientific) is made of stainless steel fitted with 2.0-mm-thick CaF_2 windows. Optical path lengths through the sample range from 250 μm to 1 mm. The sample cell is mounted on two sets of three-axis translation stages, one set is manually driven and one set is computer controlled (Standa), for both alignment purposes and prevention of photoproduct build-up on cell windows during TRIR experiments. The sample concentrations are usually on the order of 5 mM; however, the concentration is often varied in 2DIR experiments to give an absorption value of 0.5–0.7 for the vibrational modes of interest.

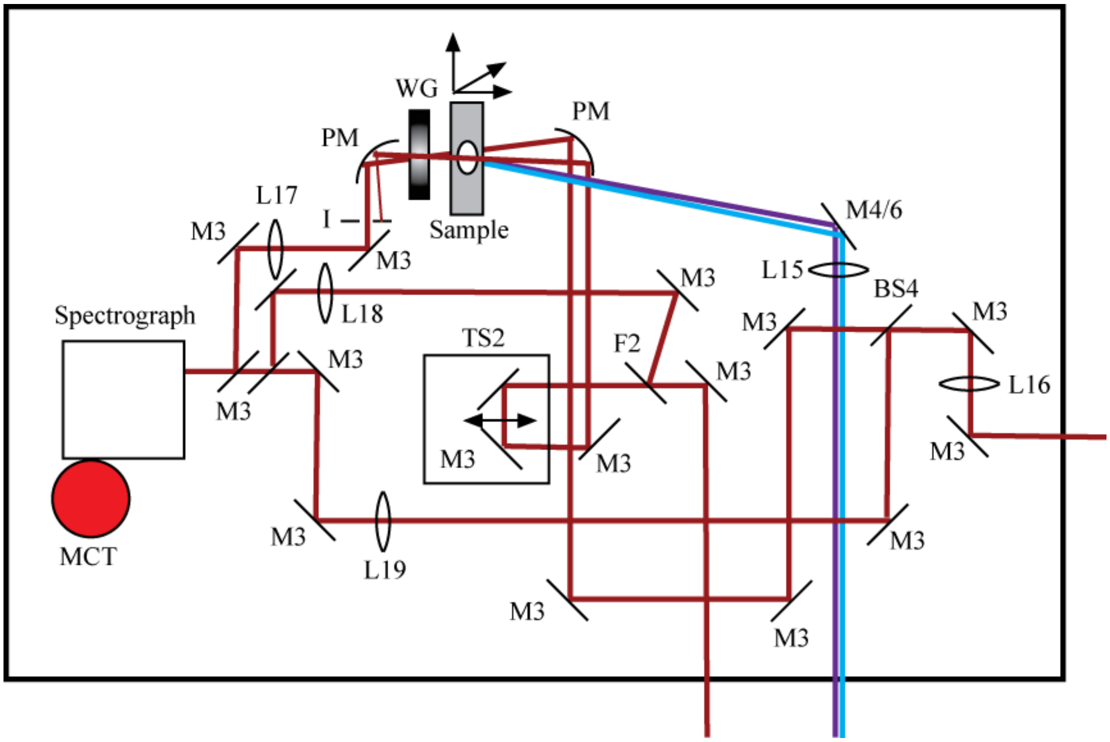

Figure 2.4 Sample line area
For details on the optical components labeled, refer to Tables 2.2–2.5. Beam colors: mid-IR (brown), 400 nm (cyan), and 266 nm (purple).

2.1.5 Detection and data analysis

The three IR beams (pump, signal, and reference) are focused into the spectrograph, two at a time and vertically displaced. Under normal operation, the entry slit width is 35–65 μm. The grating is 150 lines/mm and is blazed for 2000 cm^{-1}. The spectrograph serves to disperse the IR spectrum onto the detector. The IR spectra are measured with a custom-built 32x2 element HgCdTe array detector (AD); each element is 0.2x1 mm^2 (width by height) with a 12 μm spacing between elements. At 2000 cm^{-1}, the resolution is 2.3 cm^{-1}, and a single spectral shot spans 70 cm^{-1}. A LabView program was custom written by group members to control all optical devices on the table subsequent to the commercial laser system.

For all experiments, the spectra are collected at a frequency of 1 kHz. The pump beams are chopped such that half of the spectra recorded are of the pumped sample and half are of the unpumped sample. The first two steps of data manipulation occur within the main LabView program: (1) the signal is divided by the reference and (2) the pumped spectrum is subtracted from the unpumped spectrum. The result is a difference spectrum. This is typically performed 2000 times for each time delay between pump and signal beam. The data are then averaged, and the dynamical characteristics of the spectra are determined by fitting the peaks to Gaussians, Lorentzians, or Voigt profiles, and fitting the peak areas as a function of time to a sum of exponentials with the Levenberg-Marquardt method. A Voigt profile curve-fitting program can be found in the Appendix. All errors correspond to a 95% confidence interval.

Component Label	Description	Manufacturer
BS1	Beam splitter R=30 or 40% @ 800 nm	unknown
BS2	Beam sampler, silica plate R=2% @ 800 nm	New Source Tech. 073PW1008SQ1
BS3	Beam splitter R=20% @ 400 nm	New Source Tech. 15P400000
BS5	Fused silica window 1-mm thick	Unknown
C	Chopper	New Focus
CM1	Convex high reflector coated for 390 nm FL=–15 cm	Ealing Catalog, Inc. 349753000
CM2	Convex high reflector coated for 390 nm FL=–30 cm	Ealing Catalog, Inc. 349779000
CM3	Protected Ag concave mirror FL=25 cm	unknown
CM4	Protected Ag concave mirror FL=50 cm	unknown
DM1	Dichroic mirror R@800 nm, T@1.2–2.2 μm	RMI
DM2	Dichroic mirror R@1.2–1.7 μm, T@1.7–2.2 μm	RMI
F1	Manual flipper mount with M1	Newport
F2	Motorized flipper mounted mirror M3	
FP	Fabry-Perot interferometer assembly Piezo-Electric Kinetic Mount	Thorlabs KC1-T-PZ
HS	Harmonic Separator T>90% 800 nm, R>99% 400 nm	CVI BSR-48-1025
I	Iris aperture	

Table 2.3 List of optical components BS1 through I

Refer to Figures 2.1–2.4 for placement within the laser setup.

Component Label	**Description**	**Manufacturer**
L1	BK7 or quartz lens FL=20 cm, Ø=2.54 cm	unknown
L2	Bk7 or quartz lens FL=–5 cm, Ø=2.54 cm	unknown
L3	Quartz-SQ1 lens FL=1 m	New Source Tech.
L4	BK7 lens FL=3 cm	Ealing Catalog, Inc.
L5	BK7 achromatic doublet lens FL=3 cm	Ealing Catalog, Inc.
L6	BK7 lens FL=20 cm	Ealing Catalog, Inc.
L7	BK7 or quartz lens FL=15 cm	unknown
L8	CaF2 lens FL=5 cm	unknown
L9	BK7 or quartz lens FL=5 cm	unknown
L10	BK7 lens FL=10 cm, Ø=3cm	Photonics Components 01LDK168
L11	BK7 lens FL=3 cm, Ø=3 cm	Photonics Components 01LDX057
L12	BK7 lens FL=50 cm, Ø=4.2 cm	Photonics Components 01LDX247
L13	BK7 lens FL=20 cm, Ø=3 cm	Photonics Components 01LDX218
L14	BK7 lens FL=–50 cm, Ø=5 cm	Photonics Components 01LDX247
L15	UV-grade fused silica lens FL=30 cm	Newport SPX030AR.10
L16	CaF2 lens FL=50 cm	unknown
L17	CaF2 lens FL=15 cm	unknown
L18	CaF2 lens FL=35 cm	unknown
L19	CaF2 lens FL=30 cm	unknown

Table 2.4   List of lenses
Refer to Figures 2.1–2.4 for placement within the laser setup

Component Label	Description	Manufacturer	
M1	800-nm High Reflector R>99.4%, Ø=2.54 cm	RMI	
M2	800-nm High Reflector R>99.4%, 2.54x10.16cm^2	RMI	
M3	Protected Ag mirror R>95% for 0.6–1.0 μm	CVI PS-PM-1037-C	
M4	400-nm High Reflector R>99%	CVI TLM1-400-45-UNP-1025	
M5	Broadband mirror R>98.5%, 0–45°, 350–1100 nm	CVI BBDS-PM-1037-C	
M6	266-nm High Reflector R>99%	CVI Y4-1025-45-UNP	
M7	Broadband low GVD ultrafast mirror 700–825 nm, Ø=2.54 cm	unknown	
M8	Protected Au mirror R>96% 0.65–20 μm	Newport 05D20RE.4	
MCT	HgCdTe 32x2 element IR array detector	InfraRed Associates	
MM	Motorized Stability Mount	New Focus 8816-6	
PM	Off-axis parabolic mirror, protected Au coating, effective FL=10.16 cm	Janos Tech.	
PS	Periscope assembly with M1	Thorlabs	
S	C-axis cut sapphire window	Int. Sci. Prod.	
SiO2	Q0 fused silica rod l=25 cm, Ø=2.54 cm	Schott Glass North America	
Spectrograph	150 lines/mm grating blazed for 2000cm^{-1}	Acton	
TS1	Translation stage l=30 cm, step=0.1 μm	Newport IMS300CCHA	
TS1*	Translation stage l=25 cm, step=1 μm	Klinger MT-160	
TS2	Linear motor translation stage	Newport XMS-160	
WG	ZnSe wire-grid polarizer	Thorlabs WP25H-Z	
WP1	Zero-order half-wave plate	CVI QWPO-800-10-2-R15	
WP2	Zero-order half-wave plate 266 or 400 nm on computer-controlled rotation stage	CVI QWPO-266-10-2-R15 QWPO-400-10-2-R15	Newport RGV100
WP3	CdS/CdSe half-wave plate mid-IR achromatic (4.5–6 μm) on computer-controlled rotation stage	Cleveland Crystals	Newport RGV100

Table 2.5 List of optical components M1 through WP3
Refer to Figures 2.1–2.4 for placement within the laser setup.

2.2 DFT Modeling

Density functional theory (DFT) calculations are routinely performed for all TRIR and 2DIR experiments, as they are useful in modeling energetics, structures, and vibrational frequencies of ground state, transition state and intermediate species. Although unreported, DFT calculations were performed for work in Chapter 3 using Gaussian03 with the B3LYP and BP86 density functionals [71]. For work in Chapter 4, DFT calculations were performed using Q-Chem with BP86 and PBE1PBE functionals. Basis sets used for nonmetals were typically 6-31G(d), 6-31+G(d), or 6-31+G(2df), and for transition metals LANL2DZ, which uses an effective core potential to reduce computational expenses [72]. In some cases, anharmonically corrected vibrational frequencies were calculated. The work in Chapter 4 was performed in collaboration with Robert A. DiStasio, Jr., Stephen Elkind, Prof. Martin Head-Gordon, and Prof. Alex Bell at the University of California, Berkeley. Further details of the calculations are presented in Chapter 4.

3 Photochemistry of $V(CO)_6$ in Silane

3.1 Introduction

Silane activation is the first step in hydrosilation, the addition of a Si–H moiety across a double bond, typically C=C or C=O. Hydrosilation is important to a variety of industrial applications [73]

Because the silane bond strength is in the range of 90–100 kcal/mol, a catalyst is often used to activate (weaken) the Si–H bond, making the hydrosilation reaction more easily performed. To activate a Si–H bond with a transition metal catalyst, the metal must insert into the Si–H bond to form a three-center, two-electron bond. As has been shown in previous studies the spin state of the metal will dictate how strongly it will coordinate to an alkyl or a silyl moiety [11].

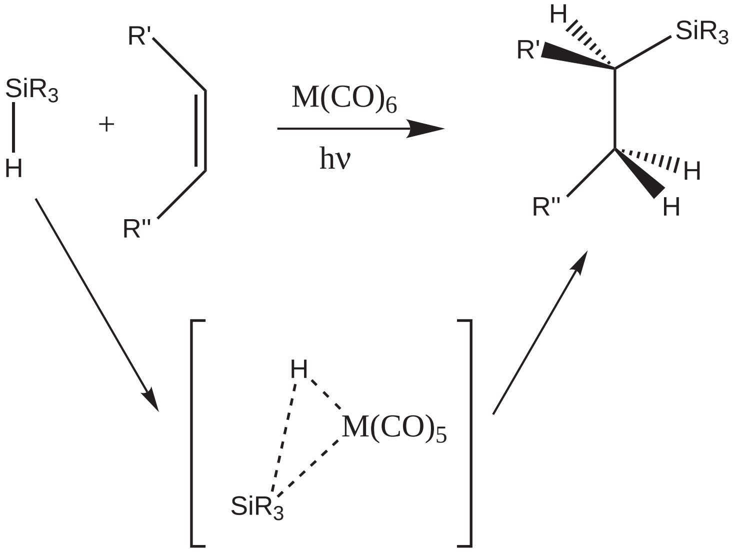

Figure 3.1 Hydrosilation.
Schematic diagram of catalyzed hydrosilation involving a silane-activated intermediate.

Coordinatively unsaturated low-spin $M(CO)_5$ (M = Cr, Mo, W) complexes have a much stronger interaction with the silyl moiety (ca. 25 kcal/mol) than with the alkyl (ca. 10 kcal/mol) [74, 75]. Similarly, CpRh(CO) (where Cp = cyclopentadienyl) demonstrates early formation of both the alkyl- and silyl-solvated species; the alkyl solvate is a long-lived intermediate on the path to formation of the silyl-solvated final product. In contrast, $Fe(CO)_4$ appears to exist only as a triplet and, consequently, does not form a stable intermediate with the alkyl. Of the species that form triplets studied by the Harris Group [9, 14], $Fe(CO)_4$ is the slowest to activate silane; this is due to the larger classical barrier to spin crossover (1.73 kcal/mol at $r_{Fe-Si} = 3.9$ Å) and small spin-orbit coupling (2.6 cm^{-1}). CpCo(CO), $CpV(CO)_3$, and $CpMn(CO)_2$ were also studied, and, upon their creation by photolysis, they all form both singlet and triplet species. Both the cobalt and manganese complexes have large spin-orbit coupling (170 and 232 cm^{-1}, respectively) and are quickly solvated by silyl. The vanadium species is slower to form the silyl solvate than the cobalt and manganese species but faster than the iron species. Its spin-orbit coupling is also intermediate (46 cm^{-1}), but it undergoes the spin crossover at the longest distance (4.3 Å). [12]

The question remains as to why metals with a triplet spin state coordinate strongly to Si–H bonds and not to C–H bonds [76-80]. It has been suggested that the energetics of the unpaired electrons of the triplet species are a better match for the silane bond, contributing to a stronger bonding interaction. One could also speculate that the unpaired electrons in the triplet species are better able to insert into the silane, given that, only in the triplet species, are there frontier electrons not involved in bonding. If a single unpaired electron is able to effect the strong coordination of a transition metal complex to a silane bond, then a doublet species should exhibit similar behavior. Otherwise, the presence of the second electron must be needed, and the reaction can be fully described as a concerted solvation and spin crossover mechanism in the ultrafast time regime. This latter description contrasts with the generally held observation that reactions involving spin crossover are slowed.

$V(CO)_6$ is a doublet before and after photodissociation of one carbonyl ligand. In other respects, it is similar to the compounds previously studied by the Harris Group: $CpV(CO)_4$ and $Fe(CO)_5$. As $V(CO)_6$ and $CpV(CO)_4$ have the same metal center, the unpaired electons should occupy similarly shaped orbitals, which should make the sterics of insertion into the silane similar. $V(CO)_6$ and $Fe(CO)_5$ are both homoleptic metal carbonyls.

$V(CO)_6$ is a doublet because it only has seventeen electrons in its valence shell. As such, it breaks the "18-electron rule," which is derived from the fact that the 18-electron configuration in the valence shell is the most stable for d-block metals as it is with eighteen electrons that the valence shell is filled [48]. The 18-electron rule is the d-block equivalent to the more familiar octet rule. $V(CO)_6$ is unique in that it is the only stable 17-electron homoleptic metal–carbonyl species, although "stable" is a relative term. Oxygen, light, heat, and most polar solvents can cause decomposition.

3.2 Methods

$V(CO)_6$ and its anion precursor were not commercially available at the time of this study. Dr. Richard Andersen of the Chemistry Department at the University of California, Berkeley, had a small amount of precursor and was kind enough to contribute both it and the assistance of his student Marc Walter for synthesis.

3.2.1 Sample preparation

The procedure of Silvestri et al. was followed to convert the diglyme-stabilzed sodium hexacarbonyl vanadate salt to vanadium hexacarbonyl [81]. First we converted the diglyme-stabilized sodium hexacarbonyl vanadate, through a cation exchange, to tetraethylammonium hexacarbonyl vanadate, an orange powder.

$$\mathrm{[Na(diglyme)_2][V(CO)_6] + Et_4NBr} \xrightarrow[\mathrm{EtOH\ /\ H_2O}]{\text{acetone /}} \mathrm{[Na][V(CO)_6] + NaBr + 2diglyme}$$

The product was kept under an inert atmosphere in a freezer away from light until the time of the spectroscopic experiments. At that time, the vanadate salt was oxidized with orthophosphoric acid under vacuum

$$\mathrm{[Et_4N][V(CO)_6] + H_3PO_4} \xrightarrow{40\ ^{\circ}\mathrm{C}} \mathrm{V(CO)_6 + [Et_4N][H_2PO_4]} + \tfrac{1}{2}\,\mathrm{H_2}$$

to create $V(CO)_6$, a lustrous black solid, which was collected in a trap cooled with liquid-N_2. The product was transferred to an inert-atmosphere glovebox and dissolved in triethylsilane, producing a yellow solution.

The sample was then held under nitrogen or argon, away from light, and chilled with dry ice for the duration of the spectroscopic experiments (ca. 2 hours until decomposition).

3.3 Results and Discussion

As $V(CO)_6$ undergoes dynamic Jahn-Teller distortion on the IR timescale, it can be approximated as having octahedral geometry. Therefore, the IR absorption spectrum of $V(CO)_6$ in triethylsilane shows only one carbonyl stretching mode at 1973 cm^{-1}. For the ultrafast transient IR spectroscopic experiments, the sample was pumped with 266-nm light. The resulting spectra are shown in Figure 3.2. Within this spectral range there are only two series of peaks: the parent bleach at 1973 cm^{-1} and the product/hot parent peak around 1930 cm^{-1}. If an analogy to previous work can be make, any silyl solvate would appear between 1930 and 2050 cm^{-1}. Unfortunately, we have no estimated frequencies from computation as no DFT studies of the parent and potential products converged. Without more data, specifically a broader spectrum, no definitive conclusions can be drawn.

Synthesis provided only enough sample to collect two sets of time-resolved spectra. The first is shown here, and the second is unusable as a result of laser alignment issues. Further study is unfeasible due to lack of available synthetic precursor.

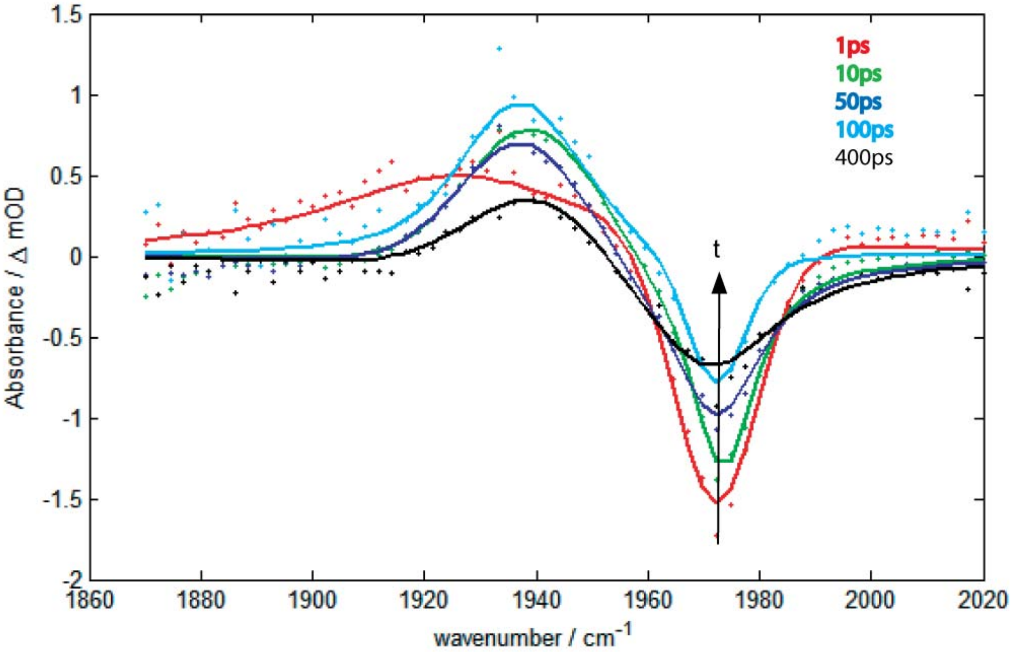

Figure 3.2 Transient IR Spectra of $V(CO)_6$.
Data points are represented as dots, and Voigt-profile fits to the data are represented as solid curves. The arrow indicates reformation of the parent complex as bleach depletion.

4 Fluxionality in $Fe_3(CO)_{12}$ and $Ru_3(CO)_{12}$

4.1 Introduction

In the study of chemical reactions, characterization of the transition state could be called one of the "Holy Grails." The reason comes both from the importance of transition states to the understanding of the nature of chemical reactions and from the challenge of determining the structure of a species whose lifetime is nearly infinitesimal. Most methods for studying chemical reactions can characterize only molecules of finite lifetimes, e.g. the so-called "transient intermediates" [82]. The data from these studies indicates, primarily, the structures of the molecules at local minima on the potential energy surface. However, only at the instances when the molecules move out of the minima and pass over the transition states do chemical reactions occur. To understand a chemical reaction, then, one must characterize the geometry of the transition state, a task of which most experimental techniques are incapable. As an exception to these, Transition State Spectroscopy can provide a, more-or-less, complete picture of a reaction mechanism by directly probing the electronic states involved, but it is limited to the gas phase and requires a detailed understanding of the potential energy surfaces [83-86].

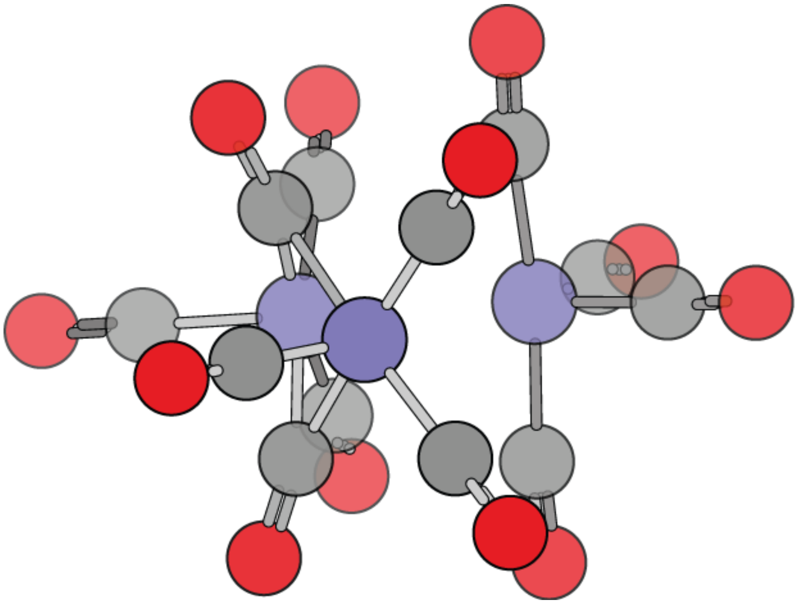

Figure 4.1 $Fe_3(CO)_{12}$ Structure
Ground state geometry of $Fe_3(CO)_{12}$ as determined by DFT.

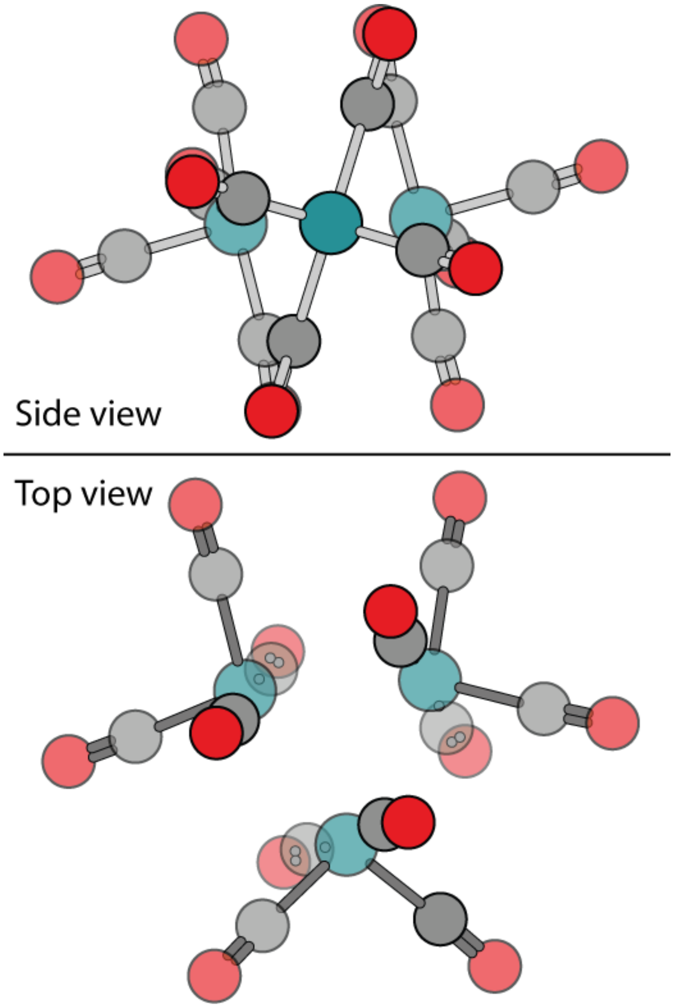

Figure 4.2 $Ru_3(CO)_{12}$ Structure
Ground state geometry of $Ru_3(CO)_{12}$ as determined by DFT.

Recent work from the Harris group has demonstrated that two-dimensional infrared spectroscopy (2DIR) can also provide structural information on the transition state of a thermal reaction, fluxionality in $Fe(CO)_5$ [54]. Here we will use 2DIR to determine the fluxional mechanisms of metallo-carbonyl clusters of the formula $M_3(CO)_{12}$ (M = Fe or Ru); refer to Figures 4.1 and 4.2 for ground state geometries. Fluxionality is a process whereby a molecule rearranges between chemically indistinguishable structures. Although there is no chemical difference between initial and final states of a fluxional reaction, their study does provide information on fundamental aspects of condensed-phase reactivity and molecular behavior. In particular, the study of reactivity in metal clusters complements chemisorption and catalytic studies of metal surfaces *in vacuo*[16-25, 29, 87-121].

Since the early years of research on fluxional molecules, metallo-carbonyl clusters have been among the systems of interest. Not only are the clusters larger than the prototypical $Fe(CO)_5$, but they also have many more proposed fluxional mechanisms and a greater chance that multiple mechanisms are occurring simultaneously. Their fluxional mechanism often has very low barriers, and this hinders their study by NMR techniques

[21, 91, 97, 108]. When cluster fluxionality is studied by NMR, the carbonyl ligands are partially substituted. The purpose is to slow the reaction or provide a tag; obviously, this can lead to changes in the details of the fluxional mechanism. However, much thought has gone into this question, and, apparent from the literature, there are two camps on how to approach the answer. The first uses the easily comprehended Local Bonding Model where the breaking and formation of M–CO bonds is highlighted. In this picture the metal center is essentially stationary (excepting for changes in M–M distances) and the carbonyl ligands change position both on a single metal atom and between two adjacent metal atoms [22]. This relies on a traditional view of the cluster as a molecule of atoms and bonds. The second camp uses the Ligand Polyhedral Model where the ligands are viewed on whole as a polyhedron [18, 24]. In this representation, the ligand polyhedron either does not move or merely shifts to a different polyhedron (see Figure 4.3 for an example) while the metal triangle tilts or twists within. There also exists disagreement on whether these two approaches are merely two ways of representing identical processes, however, the Ligand Polyhedral Model camp does taut its inclusion in Cotton and Wilkinson's *Advance Inorganic Chemistry, 5th ed.* as validation.

As with this study, the focus of most research on cluster fluxionality has centered on $M_3(CO)_{12}$ (M = Fe, Ru) and their derivatives. Additionally, there have been studies on the fluxionality of $Os_3(CO)_{12}$ and its derivatives, but, given the similarity of its ground state configuration to the ruthenium cluster and the similarity in size of osmium and ruthenium, one may reasonably assume that $Ru_3(CO)_{12}$ and $Os_3(CO)_{12}$ share similar fluxional mechanisms. For $Fe_3(CO)_{12}$, the concerted bridge-opening, bridge-closing mechanism of the Local Bonding Model and the librational mode mechanism of the Ligand Polyhedral Model are predicted to be the lowest energy fluxional mechanisms of each set, and, as shown in Figure 4.4, they represent the identical exchange of carbonyls [23]. For $Ru_3(CO)_{12}$, the lowest fluxional barrier measured by NMR falls in the range 3.9–5.4 kcal/mol. Separately, the Ligand Polyhedron Model predicts that the lowest energy transition state geometry has the carbonyls arranged in a anticubeoctahedron. As for the Local Bonding Model, no consensus exists on the lowest energy transition state geometry.

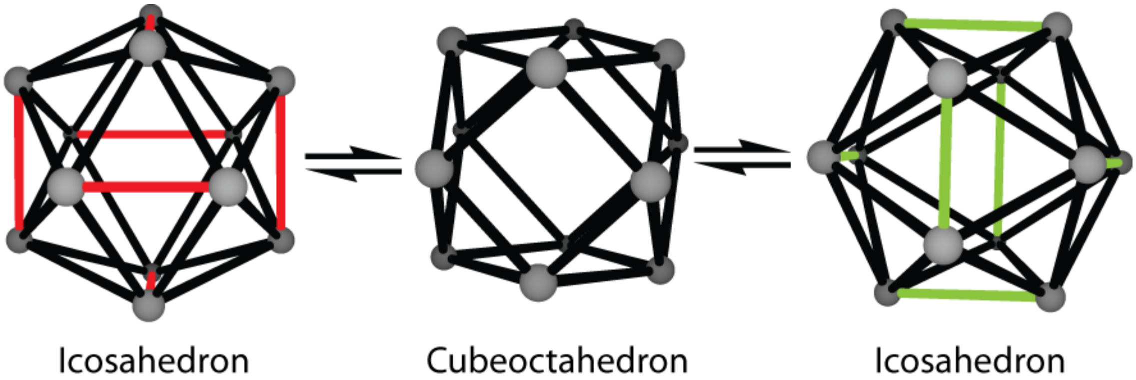

Figure 4.3 Polyhedral rearrangement
An example of polyhedral rearrangement in the Ligand Polyhedral Model. Edges marked with red in the icosahedron on the left break during conversion to the cubeoctahedron.

Edges marked with green in the icosahedron on the right form during conversion from the cubeoctahedron.

Two-dimensional infrared spectroscopy is uniquely poised to answer questions about these low energy barriers [28]. By exciting a single vibrational mode and tracking how that energy is redistributed among the other modes with picosecond time resolution, we can determine which ligands are exchanged and the timescale of that process. With that information we can determine the exact nature of the transition state, as was shown by Cahoon et al. In that study, we concluded that $Fe(CO)_5$ does indeed undergo the Berry pseudorotation with a transition state barrier of ca. 2 kcal/mol [54]. There exist a number of differences between that study and this. The first being the fluxional mechanism of $Fe(CO)_5$ does not break or form bonds as will any exchange of carbonyls between metal atoms. The second being the vibrational modes of $Fe(CO)_5$ involve two sets of carbonyl stretches. The a_2'' band is the antisymmetric stretch of the axial carbonyls, and the e' band is the antisymmetric stretch of equatorial carbonyls. In the metal clusters, a carbonyl is typically involved in multiple stretching modes. These differences may complicate vibrational tracking by 2DIR. . In the case of these metal clusters, spectral congestion made use of transient resonance 2DIR unfeasible, and low concentration of the bridged ground state in solution phase made detection by this laser apparatus impossible. Hence, we turned away from experimental methods completely in favor of computation.

The $Fe(CO)_5$ study failed to converge any alternate transition state structures by DFT. In anticipation of similar problems, we have engaged a recently developed computational method called Growing String (GSM) to find potential transition state geometries. Simply put, GSM works over the top of a DFT and requires of the user only the initial and final structures to find the reaction mechanism [26, 27, 65-67]. It accomplishes this by interpolating a line in coordinate space between initial and final geometries, then finding intermediate structures which then undergo a partial geometry optimization to minimize their energy orthogonal to the predicted reaction path. Eventually, the lowest energy path is found along which are evenly spaced "nodes" corresponding to intermediate structures; the highest energy node corresponds to the transition state in simple reactions. As would be predicted by the Hammond–Leffler Postulate, the center node in the reactions studied here corresponds to the transition state. Given the initial and final structures are chemically indistinguishable, they are isoenergetic; therefore the reaction path is symmetric in energy.

With the information from the computational work finding the energies and geometries of the potential transition states, we can immediately rule out any that have unreasonably high barriers for our time regime. We can then match the timescales of the vibrational energy redistribution measured by experiment to the possible mechanisms provided by GSM to conclusively identify the fluxional mechanisms of $Fe_3(CO)_{12}$ and $Ru_3(CO)_{12}$.

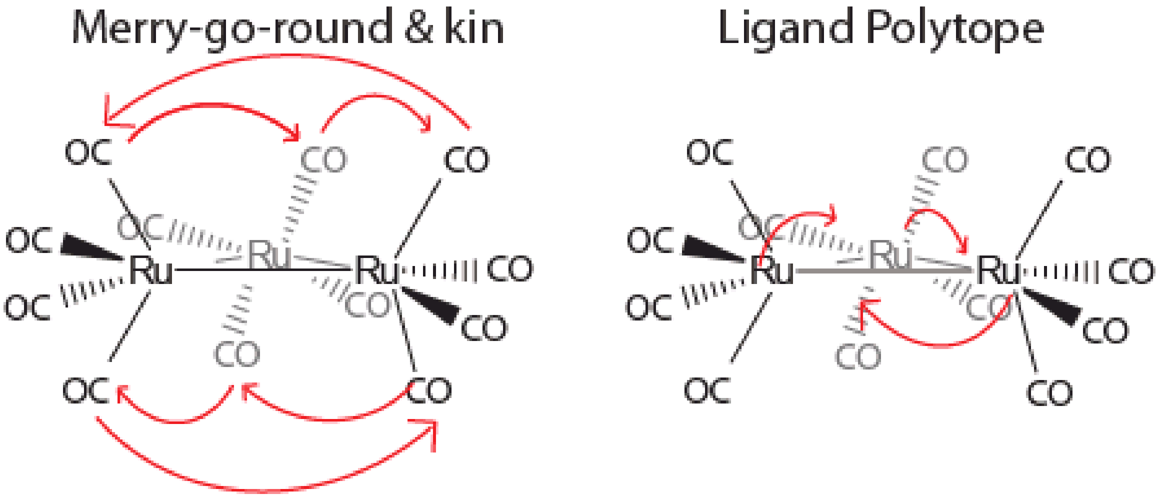

Figure 4.4 Simplified LBM/LPM Comparison.
One may view the ligands as stationary and the metals static in the Local Bonding Model (right) and the metals as stationary and the ligands static in the Ligand Polyhedron Model.

4.2 Computational Methods

4.2.1 DFT modeling

For ease of understanding, the mechanisms studied are presented in a way that resembles the Local Bonding Model. The DFT modeling, including all work done using the Growing String Method, performed for this project was done by Robert A. DiStasio, Jr., former member of Martin Head-Gordon's research group, and Stephen Elkind, joint member of Martin Head-Gordon's and Alex Bell's research groups in the Chemistry Department at the University of California, Berkeley. A description of the computational methods used is included below.

DFT calculations were carried out with the program package Q-Chem version 3.2, and using the BP86 density function. Basis sets for carbon and oxygen were 6-31G*, and for iron and ruthenium LANL2DZ which includes a relativistic effective core potential. Ground state geometries were calculated using the strictest criteria. Growing string method was built into Q-Chem as a separate option. The inputs for the GSM calculation were the initial and final structures, as well as final number of nodes and DFT particulars. The final structure was made by reordering the Cartesian coordinate file so that specific carbonyls would exchange places in the manner they would had they undergone the desired mechanism. In this way each mechanism was calculated separately. The renumbering of carbonyls is a straightforward process (see Tables 4.1 and 4.2), except in the case of the concerted bridge-opening, bridge-closing (CBOBC) mechanism for

$Fe_3(CO)_{12}$. Because the bridged metals do not remain constant, the final structure happens to have also undergone a ca. 120° rotation about the axis normal to the plane of the iron atoms.

The GSM calculation is normally terminated early, so that computing power can be focused solely on the highest energy node (the one presumed to lie closest to the transition state geometry). A frequency calculation is performed to confirm that the structure has only one imaginary frequency whose motion resembles the reaction mechanism. This can be confirmed by performing two intrinsic reaction coordinate calculations that "nudge" the structure either direction of the motion of the imaginary frequency; the structure should then converge to the correct initial and final geometries.

The mechanisms termed "pseudo-N rotation" involve all terminal carbonyls of one metal atom rotating about the metal in a pinwheel-type motion. The concerted bridge-opening, bridge-closing (CBOBC) mechanism involves all twelve carbonyls changing position; it is visualized in Figure 4.6 and is isomorphic with the LPM mechanism shown in Figure 4.3 Only the carbonyls bound to the bridged iron atoms change position in the aptly named Cotton's Merry-Go-Round (CMGR) mechanism—visualized also in Figure 4.6. . It is interesting to note that the transition state geometry for the CMGR mechanism resembles the ground state structure of the triruthenium complex, which is why one of the mechanisms for fluxionality in $Ru_3(CO)_{12}$ is called "shifted CMGR" as its transition state resembles the ground state of $Fe_3(CO)_{12}$. All the μ-3 type mechanisms involve an axial carbonyl on the unbridged iron moving directly into a bridging slot, where the intermediate presumably has a μ-3 bound carbonyl atop the iron triangle.

Fluxional Mechanisms for Iron		**Barrier Height by GSM (kcal/mol)**
On a Single Iron Atom		
Nonbridged Fe		
Pseudo-3 rotation (1 of 2)	$(CO)_9 \rightarrow (CO)_{10} \rightarrow (CO)_{12} \rightarrow (CO)_9$	<17.2
Pseudo-4 rotation	$(CO)_9 \rightarrow (CO)_{10} \rightarrow (CO)_{11} \rightarrow (CO)_{12} \rightarrow (CO)_9$	Unconverged
Bridged Fe		
Pseudo-3 rotation (1 of 2)	$(CO)_3 \rightarrow (CO)_4 \rightarrow (CO)_5 \rightarrow (CO)_3$	<15.0
Among Iron Atoms		
Lower barrier		
Concerted bridge-opening, bridge-closing	$Fe_1 \rightarrow Fe_2 \rightarrow Fe_3 \rightarrow Fe_1$ $(CO)_1 \rightarrow (CO)_6 \rightarrow (CO)_9 \rightarrow (CO)_1$ $(CO)_2 \rightarrow (CO)_{11} \rightarrow (CO)_4 \rightarrow (CO)_2$ $(CO)_3 \rightarrow (CO)_7 \rightarrow (CO)_{10} \rightarrow (CO)_3$ $(CO)_5 \rightarrow (CO)_8 \rightarrow (CO)_{12} \rightarrow (CO)_5$	0.777
Cotton's merry-go-round	$(CO)_1 \rightarrow (CO)_3 \rightarrow (CO)_4 \rightarrow (CO)_2 \rightarrow (CO)_8$ $\rightarrow (CO)_6 \rightarrow (CO)_1$	4.285
μ-3 type		
Highly hindered	$(CO)_1 \rightarrow (CO)_9 \rightarrow (CO)_{11} \rightarrow (CO)_{12} \rightarrow (CO)_1$	Did not converge
Single twist	$(CO)_1 \rightarrow (CO)_9 \rightarrow (CO)_{10} \rightarrow (CO)_{11} \rightarrow (CO)_2$ $\rightarrow (CO)_1$	
Double twist (*cis*)	$(CO)_1 \rightarrow (CO)_9 \rightarrow (CO)_{10} \rightarrow (CO)_{11} \rightarrow (CO)_2$ $\rightarrow (CO)_7 \rightarrow (CO)_1$	
Double twist (*trans*)	$(CO)_1 \rightarrow (CO)_9 \rightarrow (CO)_{10} \rightarrow (CO)_{11} \rightarrow (CO)_2$ $\rightarrow (CO)_5 \rightarrow (CO)_1$	

Table 4.1 Fluxional Mechanisms for Iron

Fluxional Mechanisms for Ruthenium		
On a Single Ruthenium Atom		
	Pseudo-3 rotation (1 of 6)	$(CO)_4 \rightarrow (CO)_{10} \rightarrow (CO)_6 \rightarrow (CO)_4$
	Pseudo-4 rotation (1 of 3)	$(CO)_4 \rightarrow (CO)_{10} \rightarrow (CO)_8 \rightarrow (CO)_6 \rightarrow (CO)_4$
Among Ruthenium Atoms		
	Concerted axial-equatorial exchange	$(CO)_4 \rightarrow (CO)_{14} \rightarrow (CO)_{12} \rightarrow (CO)_{22} \rightarrow (CO)_{20} \rightarrow (CO)_6 \rightarrow (CO)_4$ $(CO)_8 \rightarrow (CO)_{26} \rightarrow (CO)_{24} \rightarrow (CO)_{18} \rightarrow (CO)_{16} \rightarrow (CO)_{10} \rightarrow (CO)_8$
	Shifted Cotton's merry-go-round	$(CO)_4 \rightarrow (CO)_{12} \rightarrow (CO)_{18} \rightarrow (CO)_{16} \rightarrow (CO)_8 \rightarrow (CO)_6 \rightarrow (CO)_4$
	Axial exchange	$(CO)_4 \rightarrow (CO)_{12} \rightarrow (CO)_{20} \rightarrow (CO)_4$ $(CO)_8 \rightarrow (CO)_{24} \rightarrow (CO)_{26} \rightarrow (CO)_8$
	Flop via D_{3h} transition state	Axial ligands: /// → \\\
	Combined flop and axial exchange	See previous two mechanisms

Table 4.2 Fluxional Mechanisms for Ruthenium

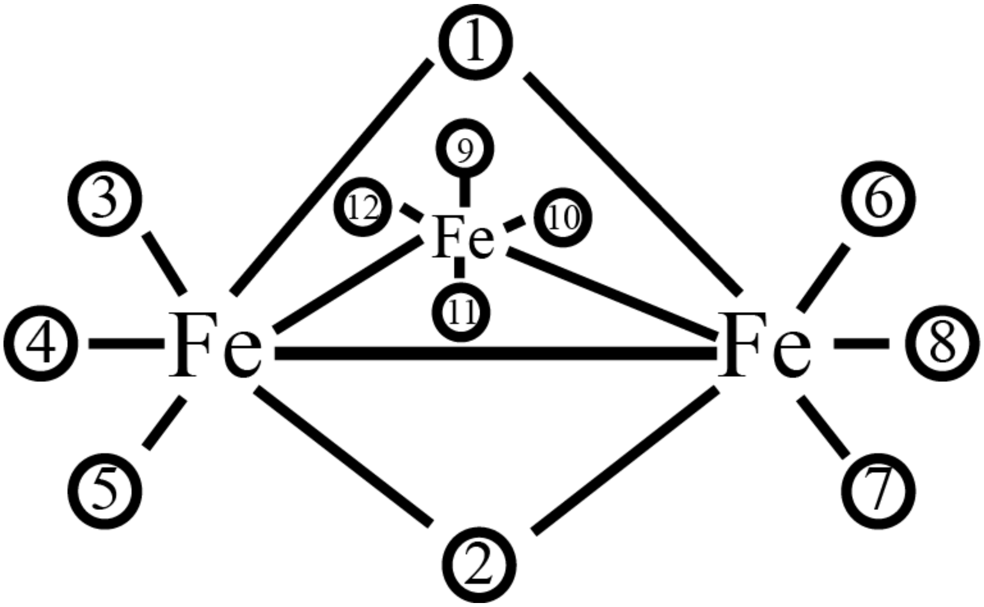

Figure 4.5 Carbonyl Numbering Scheme for $Fe_3(CO)_{12}$.
In the work presented, all carbonyl ligands used this numbering scheme. $(CO)_1$ and $(CO)_2$ are the bridging carbonyls.

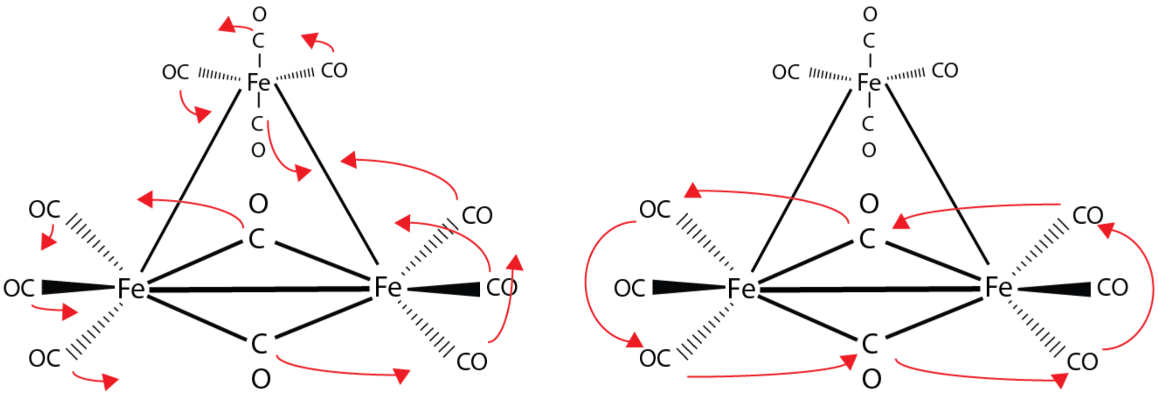

Figure 4.6 Two Contender Mechanisms
Diagram of the Concerted Bridge-Opening, Bridge-Closing Mechanism (left) and the Cotton's Merry-Go-Round Mechanism (right). Geometry shown is the initial ground state. Arrows point to position of motion for each mobile carboxyl ligand. Note that the CBOBC mechanism results in a return to the ground state geometry, however it is rotated ca. 120° around the axis normal to the plane of the metals.

4.3 Results and Discussion

Firstly, no calculations converged for the triruthenium cluster; current work is progressing using the subsequent version of GSM called "Freezing String Method." The reader will note that certain mechanisms for the triiron cluster were halted prematurely; this was done as it became clear that they were converging to a relatively high-energy transition state. The two most important mechanisms, for this work and work published by others, are the concerted bridge-opening, bridge-closing (CBOBC) and Cotton's Merry-Go-Round (CMGR). In the former, all ligands change position during the reaction, and, indeed, the bridging site moves from one side of the metal triangle to another side. This author speculates that favorable interactions among the ligands contribute to the very low energy barrier (0.777 kcal/mol) to this reaction. Each ligand pushes its neighbors, and all orbital interactions are being altered. The use of the semi-empirical basis set PBE1PBE may alter the calculated energy barrier as it incorporates dispersion effects—in this case orbital interactions between neighboring carbonyl ligands. The CMGR mechanism involves motion only among carbonyls around the bridging site. Its calculated energy barrier is 4.285 kcal/mol, significantly higher than the barrier for the CBOBC mechanism.

This study offers the first evidence of barrier heights for several fluxional mechanisms for $Fe_3(CO)_{12}$. The reaction with the lowest barrier is CBOBC with an value of 0.777 kcal/mol. Such a low barrier may explain the low intensity in the IR for the ground state vibrations.

5 Conclusions

The studies presented here cover two very different approaches to molecular dynamics. The first study investigated whether an organometallic doublet would react on the sub-1-ns timescale. Photoinitiation by an ultraviolet pulse was required to determine the dynamics of the generated intermediate species, of which there were none. While organometallic triplets favor silicon–hydrogen bonds and singlets react quickly with carbon–hydrogen bond, it appears that doublets are unreactive on the ultrafast timescale. Ultrafast time-resolved spectroscopy can be a valuable tool in collecting evidence of a reaction mechanism, and it is often accompanied by computational modeling of the chemical species. The latter study presented a case experimentally hindered by detection limits but whose computational results presented a clear answer as to which of the many proposed reaction mechanisms occurs on an ultrafast timescale: concerted bridge-opening, bridge-closing of $Fe_3(CO)_{12}$ with an energy barrier of 0.777 kcal/mol compared to the next lowest mechanism of Cotton's Merry-Go-Round with an energy barrier of 4.285 kcal/mol. The iron- and ruthenium-cluster study leaves a few questions unanswered, the most important being whether including orbital interactions between neighboring ligands would alter the calculated energy barrier.

Bibliography

1. **Breene, R. G., Jr., *Theories of Spectral Line Shape*. Wiley: New York, 1981.**

2. **Glascoe, E. A.; Sawyer, K. R.; Shanoski, J. E.; Harris, C. B., *J. Phys. Chem. C* 2007, *111* (25), 8789-8795.**

3. **Glascoe, E. A.; Kling, M. F.; Shanoski, J. E.; Harris, C. B., *Organometallics* 2006, *25* (3), 775-784.**

4. **Sawyer, K. R.; Glascoe, E. A.; Cahoon, J. F.; Schlegel, J. P.; Harris, C. B., *Organometallics* 2008, *27* (17), 4370-4379.**

5. **Sawyer, K. R.; Steele, R. P.; Glascoe, E. A.; Cahoon, J. F.; Schlegel, J. P.; Head-Gordon, M.; Harris, C. B., *Journal of Physical Chemistry A* 2008.**

6. **Shanoski, J. E.; Glascoe, E. A.; Harris, C. B., *Journal of Physical Chemistry B* 2006, *110* (2), 996-1005.**

7. **Asplund, M. C.; Snee, P. T.; Yeston, J. S.; Wilkens, M. J.; Payne, C. K.; Yang, H.; Kotz, K. T.; Frei, H.; Bergman, R. G.; Harris, C. B., *Journal of the American Chemical Society* 2002, *124* (35), 10605-10612.**

8. **Lian, T. Q.; Bromberg, S. E.; Asplund, M. C.; Yang, H.; Harris, C. B., *Journal of Physical Chemistry* 1996, *100* (29), 11994-12001.**

9. **Yang, H.; Asplund, M. C.; Kotz, K. T.; Wilkens, M. J.; Frei, H.; Harris, C., *Journal of the American Chemical Society* 1998, *120* (39), 10154-10165.**

10. **Yang, H.; Kotz, K. T.; Asplund, M. C.; Wilkens, M. J.; Harris, C. B., *Accounts of Chemical Research* 1999, *32* (7), 551-560.**

11. **Kotz, K. T.; Yang, H.; Snee, P. T.; Payne, C. K.; Harris, C. B., *Journal of Organometallic Chemistry* 2000, *596* (1-2), 183-192.**

12. **Snee, P. T.; Payne, C. K.; Kotz, K. T.; Yang, H.; Harris, C. B., *Journal of the American Chemical Society* 2001, *123* (10), 2255-2264.**

13. **Snee, P. T.; Shanoski, J.; Harris, C. B., *Journal of the American Chemical Society* 2005, *127* (4), 1286-1290.**

14. **Snee, P. T.; Payne, C. K.; Mebane, S. D.; Kotz, K. T.; Harris, C. B., *Journal of the American Chemical Society* 2001, *123* (28), 6909-6915.**

15. Cotton, F. A.; Danti, A.; Waugh, J. S.; Fessenden, R. W., *Journal of Chemical Physics* 1958, *29* (6), 1427-1428.

16. Johnson, B. F. G., *J Chem Soc Dalton* 1997, (9), 1473-1479.

17. Johnson, B. F. G.; Roberts, Y. V., *J Chem Soc Dalton* 1993, (19), 2945-2950.

18. Johnson, B. F. G.; Roberts, Y. V., *Polyhedron* 1993, *12* (9), 977-990.

19. Johnson, B. F. G.; Roberts, Y. V.; Parisini, E., *J Chem Soc Dalton* 1992, (17), 2573-2578.

20. Johnson, B. F. G.; Tay, S., *Inorg Chim Acta* 2002, *332*, 201-203.

21. Lentz, D.; Marschall, R., *Organometallics* 1991, *10* (5), 1487-1496.

22. Mann, B. E., *Organometallics* 1992, *11* (1), 481-482.

23. Mann, B. E., *J Chem Soc Dalton* 1997, (9), 1457-1471.

24. Muettert.El, *Journal of the American Chemical Society* 1969, *91* (7), 1636-&.

25. Muettert.El, *Journal of the American Chemical Society* 1969, *91* (15), 4115-&.

26. Peters, B.; Heyden, A.; Bell, A. T.; Chakraborty, A., *Journal of Chemical Physics* 2004, *120* (17), 7877-7886.

27. Bell, A. T.; Head-Gordon, M., Quantum Mechanical Modeling of Catalytic Processes. In *Annual Review of Chemical and Biomolecular Engineering, Vol 2*, Prausnitz, J. M., Ed. 2011; Vol. 2, pp 453-477.

28. Zheng, J. R.; Kwak, K. W.; Xie, J.; Fayer, M. D., *Science* 2006, *313* (5795), 1951-1955.

29. Strauss, H. L., *Journal of the American Chemical Society* 1992, *114* (3), 905-907.

30. Nibbering, E. T. J.; Fidder, H.; Pines, E., *Annual Review of Physical Chemistry* 2005, *56*, 337-367.

31. Syage, J. A.; Felker, P. M.; Zewail, A. H., *Journal of Chemical Physics* 1984, *81* (11), 4706-4723.

32. Harris, C. B.; Shelby, R. M.; Cornelius, P. A., *Physical Review Letters* 1977, *38* (24), 1415-1419.

33. Harris, C. B.; Shelby, R. M.; Cornelius, P. A., *Chemical Physics Letters* 1978, *57* (1), 8-14.

34. Kling, M. F.; Cahoon, J. F.; Glascoe, E. A.; Shanoski, J. E.; Harris, C. B., *Journal of the American Chemical Society* 2004, *126* (37), 11414-11415.

35. Lian, T.; Bromberg, S. E.; Yang, H.; Proulx, G.; Bergman, R. G.; Harris, C. B., *Journal of the American Chemical Society* 1996, *118* (15), 3769-3770.

36. Payne, C. K.; Snee, P. T.; Yang, H.; Kotz, K. T.; Schafer, L. L.; Tilley, T. D.; Harris, C. B., *Journal of the American Chemical Society* 2001, *123* (30), 7425-7426.

37. Sawyer, K. R.; Cahoon, J. F.; Shanoski, J. E.; Webster, C. E.; Glascoe, E. A.; Andersen, L. K.; Hapke, M.; Frei, H.; Hartwig, J. F.; Harris, C. B., in preparation.

38. Sawyer, K. R.; Glascoe, E. A.; Cahoon, J. F.; Schlegel, J. P.; Harris, C. B., *Organometallics*, ASAP article.

39. Sawyer, K. R.; Steele, R. P.; Glascoe, E. A.; Cahoon, J. F.; Schlegel, J. P.; Head-Gordon, M.; Harris, C. B., *Journal of Physical Chemistry A*, in press.

40. Shanoski, J. E.; Payne, C. K.; Kling, M. F.; Glascoe, E. A.; Harris, C. B., *Organometallics* 2005, *24* (8), 1852-1859.

41. Snee, P. T.; Yang, H.; Kotz, K. T.; Payne, C. K.; Harris, C. B., *Journal of Physical Chemistry A* 1999, *103* (49), 10426-10432.

42. Yang, H.; Snee, P. T.; Kotz, K. T.; Payne, C. K.; Frei, H.; Harris, C. B., *Journal of the American Chemical Society* 1999, *121* (39), 9227-9228.

43. Yang, H.; Snee, P. T.; Kotz, K. T.; Payne, C. K.; Harris, C. B., *Journal of the American Chemical Society* 2001, *123* (18), 4204-4210.

44. Glascoe, E. A.; Kling, M. F.; Shanoski, J. E.; Harris, C. B., *Organometallics* 2006, *25* (3), 775-784.

45. DeFlores, L. P.; Nicodemus, R. A.; Tokmakoff, A., *Optics Letters* 2007, *32* (20), 2966-2968.

46. Hamm, P.; Lim, M.; DeGrado, W. F.; Hochstrasser, R. M., *Journal of Chemical Physics* 2000, *112* (4), 1907-1916.

47. Tokmakoff, A.; Sauter, B.; Fayer, M. D., *Journal of Chemical Physics* 1994, *100* (12), 9035-9043.

48. Miessler, G. L.; Tarr, D. A., *Inorganic Chemistry*. 2nd ed.; Prentice Hall: Upper Saddle River, 1999.

49. Bredenbeck, J.; Hamm, P., *Chimia* 2007, *61* (1-2), 45-46.

50. Bredenbeck, J.; Helbing, J.; Behrendt, R.; Renner, C.; Moroder, L.; Wachtveitl, J.; Hamm, P., *Journal of Physical Chemistry B* 2003, *107* (33), 8654-8660.

51. Bredenbeck, J.; Helbing, J.; Hamm, P., *Journal of the American Chemical Society* 2004, *126* (4), 990-991.

52. Bredenbeck, J.; Helbing, J.; Kolano, C.; Hamm, P., *Chemphyschem* 2007, *8* (12), 1747-1756.

53. Bredenbeck, J.; Helbing, J.; Nienhaus, K.; Nienhaus, G. U.; Hamm, P., *Proceedings of the National Academy of Sciences of the United States of America* 2007, *104* (36), 14243-14248.

54. Cahoon, J. F.; Sawyer, K. R.; Schlegel, J. P.; Harris, C. B., *Science* 2008, *319* (5871), 1820-1823.

55. Chung, H. S.; Ganim, Z.; Jones, K. C.; Tokmakoff, A., *Proceedings of the National Academy of Sciences* 2007, *104* (36), 14237-14242.

56. Finkelstein, I. J.; Zheng, J. R.; Ishikawa, H.; Kim, S.; Kwak, K.; Fayer, M. D., *Physical Chemistry Chemical Physics* 2007, *9* (13), 1533-1549.

57. Khalil, M.; Demirdoven, N.; Tokmakoff, A., *Journal of Physical Chemistry A* 2003, *107* (27), 5258-5279.

58. Khalil, M.; Demirdoven, N.; Tokmakoff, A., *Journal of Chemical Physics* 2004, *121* (1), 362-373.

59. Kim, Y. S.; Hochstrasser, R. M., *Proceedings of the National Academy of Sciences of the United States of America* 2005, *102* (32), 11185-11190.

60. Kim, Y. S.; Hochstrasser, R. M., *Journal of Physical Chemistry B* 2006, *110* (17), 8531-8534.

61. Kim, Y. S.; Hochstrasser, R. M., *Journal of Physical Chemistry B* 2007, *111* (33), 9697-9701.

62. Kurochkin, D. V.; Naraharisetty, S. R. G.; Rubtsov, I. V., *Journal of Physical Chemistry A* 2005, *109* (48), 10799-10802.

63. Kurochkin, D. V.; Naraharisetty, S. R. G.; Rubtsov, I. V., *Proceedings of the National Academy of Sciences of the United States of America* 2007, *104* (36), 14209-14214.

64. Naraharisetty, S. R. G.; Kurochkin, D. V.; Rubtsov, I. V., *Chemical Physics Letters* 2007, *437* (4-6), 262-266.

65. Goodrow, A.; Bell, A. T.; Head-Gordon, M., *Journal of Chemical Physics* 2008, *129* (17).

66. Goodrow, A.; Bell, A. T.; Head-Gordon, M., *Journal of Chemical Physics* 2009, *130* (24).

67. Goodrow, A.; Bell, A. T.; Head-Gordon, M., *Chemical Physics Letters* 2010, *484* (4-6), 392-398.

68. Glascoe, E. A. University of California, Berkeley, 2006.

69. Shanoski, J. E. University of California, Berkeley, 2006.

70. Hamm, P.; Kaindl, R. A.; Stenger, J., *Optics Letters* 2000, *25* (24), 1798-1800.

71. M.J. Frisch, G. W. T., H.B. Schlegel, G.E. Scuseria, M.A. Robb, J.R. Cheeseman, J.A. Montgomery, Jr., T.Vreven, K.N. Kudin, J.C. Burant, J.M. Millam, S.S. Iyengar, J. Tomasi, V. Barone, B. Mennucci, M. Cossi, G. Scalmani, N. Rega, G.A. Petersson, H. Nakatsuji, M. Hada, M. Ehara, K. Toyota, R. Fukuda, J. Hasegawa, M. Ishida, T. Nakajima, Y. Honda, O. Kitao, H. Nakai, M. Klene, X. Li, J.E. Knox, H.P. Hratchian, J.B. Cross, V. Bakken, C. Adamo, J. Jaramillo, R. Gomperts, R.E. Stratmann, O. Yazyev, A.J. Austin, R. Cammi, C. Pomelli, J.W. Ochterski, P.Y. Ayala, K. Morokuma, G.A. Voth, P. Salvador, J.J. Dannenberg, V.G. Zakrzewski, S. Dapprich, A.D. Daniels, M.C. Strain, O. Farkas, D.K. Malick, A.D. Rabuck, K. Raghavachari, J.B. Foresman, J.V. Ortiz, Q. Cui, A.G. Baboul, S. Clifford, J. Cioslowski, B.B. Stefanov, G. Liu, A. Liashenko, P. Piskorz, I. Komaromi, R.L. Martin, D.J. Fox, T. Keith, M.A. Al-Laham, C.Y. Peng, A. Nanayakkara, M. Challacombe, P.M.W. Gill, B. Johnson, W. Chen, M.W. Wong, C. Gonzalez, J.A. Pople *Gaussian 03, Revision C.02, Gaussian, Inc.*, Wallingford, CT, 2004.

72. Shao, Y.; Molnar, L. F.; Jung, Y.; Kussmann, J.; Ochsenfeld, C.; Brown, S. T.; Gilbert, A. T. B.; Slipchenko, L. V.; Levchenko, S. V.; O'Neill, D. P.; DiStasio, R. A.; Lochan, R. C.; Wang, T.; Beran, G. J. O.; Besley, N. A.; Herbert, J. M.; Lin, C. Y.; Van Voorhis, T.; Chien, S. H.; Sodt, A.; Steele, R. P.; Rassolov, V. A.; Maslen, P. E.; Korambath, P. P.; Adamson, R. D.; Austin, B.; Baker, J.; Byrd, E. F. C.; Dachsel, H.; Doerksen, R. J.; Dreuw, A.; Dunietz, B. D.; Dutoi, A. D.; Furlani, T. R.; Gwaltney, S. R.; Heyden, A.; Hirata, S.; Hsu, C. P.; Kedziora, G.; Khalliulin, R. Z.; Klunzinger, P.; Lee, A. M.; Lee, M. S.; Liang, W.; Lotan, I.; Nair, N.; Peters, B.; Proynov, E. I.; Pieniazek, P. A.; Rhee, Y. M.; Ritchie, J.; Rosta, E.; Sherrill, C. D.; Simmonett, A. C.; Subotnik, J. E.; Woodcock, H. L.; Zhang, W.; Bell, A. T.; Chakraborty, A. K.; Chipman, D. M.; Keil, F. J.; Warshel, A.; Hehre, W. J.; Schaefer, H. F.; Kong, J.; Krylov, A. I.; Gill, P. M. W.; Head-Gordon, M., *Physical Chemistry Chemical Physics* 2006, *8* (27), 3172-3191.

73. Renner, H. S., G.; Kleinwächter, I.; Drost, E.; Lüschow, H. M.; Tews, P.; Panster, P.; Diehl, M.; Lang, J.; Kreuzer, T.; Knödler, A.; Starz, K. A.; Dermann, K.; Rothaut, J.; Drieselman, R. , *Platinum Group Metals and Compounds*. Wiley: 2002.

74. Burkey, T. J., *Journal of the American Chemical Society* 1990, *112* (23), 8329-8333.

75. Hu, S.; Farrell, G. J.; Cook, C.; Johnston, R.; Burkey, T. J., *Organometallics* 1994, *13* (11), 4127-4128.

76. Harvey, J. N.; Carreon-Macedo, J.-L., *Journal of the American Chemical Society* 2004, *126* (18), 9.

77. Morokuma, K.; Musaev, D. G., *Journal of the American Chemical Society* 1995, *117* (2), 7.

78. Lichtenberger, D. L.; Rai-Chaudhuri, A., *Journal of the American Chemical Society* 1989, *111* (10), 3583-3591.

79. Taw, F. L.; Bergman, R. G.; Brookhart, M., *Organometallics* 2004, *23* (4), 886-890.

80. Burger, P.; Bergman, R., *Journal of the American Chemical Society;(United States)* 1993, *115* (22).

81. Ercoli, R.; Guainazzi, M.; Silvestri, G., *Chemical Communications* 1967, 927.

82. Schaffner, K.; Grevels, F. W., *J Mol Struct* 1988, *173*, 51-65.

83. Baum, P.; Yang, D. S.; Zewail, A. H., *Science* 2007, *318* (5851), 788-792.

84. Ihee, H.; Cao, J. M.; Zewail, A. H., *Angewandte Chemie-International Edition* 2001, *40* (8), 1532-+.

85. Ihee, H.; Feenstra, J. S.; Cao, J.; Zewail, A. H., *Chemical Physics Letters* 2002, *353* (5-6), 325-334.

86. Srinivasan, R.; Lobastov, V. A.; Ruan, C. Y.; Zewail, A. H., *Helvetica Chimica Acta* 2003, *86* (6), 1763-1838.

87. Adams, H.; Bailey, N. A.; Bentley, G. W.; Mann, B. E., *J Chem Soc Dalton* 1989, (9), 1831-1844.

88. Adams, H.; Carr, A. G.; Mann, B. E.; Melling, R., *Polyhedron* 1995, *14* (19), 2771-2785.

89. **Aime, S.; Dastru, W.; Gobetto, R.; Krause, J.; Milone, L., *Organometallics* 1995, *14* (9), 4435-4438.**

90. **Alex, R. F.; Pomeroy, R. K., *Organometallics* 1987, *6* (11), 2437-2446.**

91. **Bain, A. D.; Cramer, J. A., *J Magn Reson Ser A* 1993, *103* (2), 217-222.**

92. **Bain, A. D.; Cramer, J. A., *J Magn Reson Ser A* 1996, *118* (1), 21-27.**

93. **Benfield, R. E.; Johnson, B. F. G., *Transit Metal Chem* 1981, *6* (3), 131-144.**

94. **Bouman, T. D.; Duncan, C. D.; Trindle, C., *Int J Quantum Chem* 1977, *11* (3), 399-413.**

95. **Braga, D.; Grepioni, F.; Farrugia, L. J.; Johnson, B. F. G., *J Chem Soc Dalton* 1994, (20), 2911-2918.**

96. **Cotton, F. A., *Journal of Organometallic Chemistry* 1975, *100* (1), 29-41.**

97. **Cotton, F. A.; Hunter, D. L., *Inorg Chim Acta* 1974, *11* (1), L9-L10.**

98. **Cotton, F. A.; Hunter, D. L.; Lahuerta, P., *Journal of the American Chemical Society* 1974, *96* (14), 4723-4724.**

99. **Cotton, F. A.; Troup, J. M., *Journal of the American Chemical Society* 1974, *96* (13), 4155-4159.**

100. **Dobos, S.; Nunziantecesaro, S.; Maltese, M., *Inorg Chim Acta* 1986, *113* (2), 167-172.**

101. **Farrugia, L. J., *J Chem Soc Dalton* 1997, (11), 1783-&.**

102. **Farrugia, L. J.; Gillon, A. L.; Braga, D.; Grepioni, F., *Organometallics* 1999, *18* (24), 5022-5033.**

103. **Farrugia, L. J.; Rae, S. E., *Organometallics* 1992, *11* (1), 196-206.**

104. **Fischer, R. D.; Vogler, A.; Noack, K., *Journal of Organometallic Chemistry* 1967, *7* (1), 135-&.**

105. **Gansow, O. A.; Burke, A. R.; Vernon, W. D., *Journal of the American Chemical Society* 1976, *98* (19), 5817-5826.**

106. **Gillespi.P; Hoffman, P.; Klusacek, H.; Marquard.D; Pfohl, S.; Ramirez, F.; Tsolis, E. A.; Ugi, I., *Angewandte Chemie-International Edition* 1971, *10* (10), 687-+.**

107. **Grevels, F. W.; Jacke, J.; Seevogel, K., *J Mol Struct* 1988, *174*, 107-112.**

108. **Hanson, B. E.; Lisic, E. C.; Petty, J. T.; Iannaconne, G. A.,** ***Inorg Chem*** **1986,** ***25*** **(22), 4062-4064.**

109. **Johnson, B. F. G.,** ***J Chem Soc Chem Comm*** **1976, (6), 211-213.**

110. **Johnson, B. F. G.,** ***J Chem Soc Chem Comm*** **1976, (17), 703-704.**

111. **Johnston, V. J.; Einstein, F. W. B.; Pomeroy, R. K.,** ***Organometallics*** **1988,** ***7*** **(8), 1867-1869.**

112. **Koridze, A. A.; Kizas, O. A.; Astakhova, N. M.; Petrovskii, P. V.; Grishin, Y. K.,** ***J Chem Soc Chem Comm*** **1981, (16), 853-855.**

113. **Lauher, J. W.,** ***Journal of the American Chemical Society*** **1986,** ***108*** **(7), 1521-1531.**

114. **Lewis, L. N.; Caulton, K. G.,** ***Inorg Chem*** **1981,** ***20*** **(4), 1139-1142.**

115. **Manning, A. R.,** ***J Chem Soc A*** **1968, (6), 1319-&.**

116. **Noack, K.,** ***Journal of Organometallic Chemistry*** **1967,** ***7*** **(1), 151-&.**

117. **Sironi, A.,** ***Inorg Chem*** **1996,** ***35*** **(6), 1725-&.**

118. **Turner, J. J.; Gordon, C. M.; Howdle, S. M.,** ***Journal of Physical Chemistry*** **1995,** ***99*** **(49), 17532-17538.**

119. **Turner, J. J.; Grevels, F. W.; Howdle, S. M.; Jacke, J.; Haward, M. T.; Klotzbucher, W. E.,** ***Journal of the American Chemical Society*** **1991,** ***113*** **(22), 8347-8353.**

120. **Ugi, I.; Marquard.D; Klusacek, H.; Gokel, G.; Gillespi.P,** ***Angewandte Chemie-International Edition*** **1970,** ***9*** **(9), 703-&.**

121. **Wang, H. Y.; Xie, Y. M.; King, R. B.; Schaefer, H. F.,** ***Inorg Chem*** **2006,** ***45*** **(8), 3384-3392.**

Appendix: Curve-fitting Programs

The following programs are used by MATLAB in analyzing data from transient infrared spectroscopic experiments. When using Omnivoigt.m, the user manually inputs guesses for peaks in a few key timeslices, then the program automatically fits peaks to the remaining timeslices using an adaptive-constraint interpolation algorithm. The resulting fits to the data allow extraction of peak area, width and center frequency as a function of time. The program requires two files: an output of the averaged data and an output of the standard deviations of that data. The program calls on five other functions: jvoigt.m, jvoigts.m, jvoigtb.m, lswjvoigts.m, and voigt.m. The first four are reproduced here, and the latter can be any Voigt profile approximation that is a function of (x,a) where x is a grid of vector points and a the ratio of Lorentz to Doppler*sqrt(log(2)).

Omnivoigt.m

```
%OMNIVOIGT
%==================================================
%   Author:     Jacob P Schlegel
%   Version:    3.7
%   Date:       11.7.2006
%==================================================
%This program fits multiple time slices to multiple Voigt curves by
%manually inputting parameters for a number of distinct time slices
%then using an interpolation scheme to automatically fit the
%interjacent times.
%After fitting the time slices, it tracks the evolution of position and
%area of each peak.  The fitting method is a medium-scale trust region
%minimum search (fmincon).  From the Matlab help: "fmincon uses a
%Sequential Quadratic Programming (SQP) method.  In this method, a
%Quadratic Programming (QP) subproblem is solved at each iteration.  An
%estimate of the Hessian of the Lagrangian is updated at each iteration
%using the BFGS formula."  See Matlab help for more information.
%
%A description of the interpolation scheme:  The automatically fit time
%falls between two manually fit timeslices ('early' and 'last') and
%immediately after another timeslice ('Latest').  The program
%determines initial parameters for this timeslice by, first, taking an
%average of the parameters of 'early' and 'last' (weighted according
%to the current timeslice's proximity to each), then averaging that
%with the parameters of 'Latest.'  The upper and lower bounds (UB, LB)
%are determined by, first, determining the minimum (LBa) and maximum
%(UBa) values of the final parameters of 'early' and 'last,' then
%widening those bounds by adding or subtracting a percentage ('port')
%of each.  If the final parameters of 'Latest' fall between either UB
%and UBa or LB and LBa, the program further widens the boundary which
%the final parameters of 'Latest' approached. This adaptive boundary
%method is necessary if the user does not manually fit times where
%certain peaks near a maximum or minimum in their parameters.
%
%A variable glossary follows the body of the program.
%
%This program is dependent on the following programs:
```

```
%   voigt, jvoigt, jvoigtb, jvoigts, lswjvoigts
%
clear pos amp wid ver vert vrat rat n y AllParams port times inctimes
posits mantimes lgnd;
h=input('Would you like more detailed instruction (recommended for new
users)? [y/{n}] ','s');
if isempty(h),
    h='n';
end
if (h=='y')|(h=='Y'),
    help omnivoigt;
    disp('If there exists a default input, it will be displayed in
curly braces;');
    disp('  and you have only to press [Enter] to select the
default.');
end
%Inputting data and its standard deviations
filename=input('What is the filename containing the prepared data?
{Output.dat} ','s');
if isempty(filename),
    filename='Output.dat';
end
datavar=importdata(filename);
[f t]=size(datavar);
timecols=datavar(1,2:t);
sdfilename=input('What is the filename containing the standard
deviations of the data? ','s');
SDvar=importdata(sdfilename);
%Allows user to crop frequencies from data
freqrange=input('What range of frequencies should Omnivoigt fit?
{complete}');
if length(freqrange)==2,
    lofreqr=find(datavar(:,1)>freqrange(1));
    lofreq=lofreqr(1);
    hifreqr=find(datavar(:,1)<freqrange(2));
    fl=length(hifreqr);
    hifreq=hifreqr(fl);
    datavar=datavar(lofreq:hifreq,:);
    datavar=[[0 timecols];datavar];
    SDvar=SDvar(lofreq:hifreq,:);
    SDvar=[[0 timecols];SDvar];
end
[f t]=size(datavar);
%User inputs times to manually fit ('manfit')
disp('The times, in picoseconds, available to fit are:');
disp(timecols');
if (h=='y')|(h=='Y'),
    disp('Omnivoigt will only fit those times lying between two
manually fit times.');
    disp('Suggestion: when choosing manfit times, include times where
certain');
    disp('  peaks reach a maximum amplitude');
end
mantimesz=input('Enter the times to manually fit [1,50,...,800]: ');
noman=length(mantimesz);
for i=1:noman,
```

```
    mantimes(i)=find(timecols==mantimesz(i))+1;
end
picks=input('Do you wish Omnivoigt to fit all interjacent times?
[{y}/n] ','s');
%Creates matrix of times to fit split into segments by the choices of
%manfit times.  First column of 'times' is number of time slices in the
%particular segment; other columns are the column number of the times
%to autofit.
if (picks=='n')|(picks=='N'),
    clear xx yy timeval;
    disp('Enter those times to autofit between the first');
    xx=input('  two manfit times  [2,5,20,...]: ');
    yy=length(xx);
    times(1,1)=yy;
    timeval(1)=mantimesz(1);
    timeval(2:(yy+1))=xx;
    timeval(yy+2)=mantimesz(2);
    for i=1:yy,
        times(1,(i+1))=find(timecols==xx(i));
    end
    for i=2:(noman-1),
        clear xx yy;
        xx=input('Pick the next set of times: ');
        yy=length(xx);
        times(i,1)=yy;
        ltsf=length(timeval)+1;
        timeval(ltsf:ltsf+yy)=xx;
        timeval(ltsf+yy+1)=mantimesz(i+1);
        for j=1:yy,
            times(i,(j+1))=find(timecols==xx(j));
        end
    end
else
    clear timeval;
    timeval(1)=mantimesz(1);
    for i=1:(noman-1),
        clear xx yy;
        xx=(mantimes(i)+1):(mantimes(i+1)-1);
        yy=length(xx);
        times(i,1:(yy+1))=[yy,xx];
        ltsf=length(timeval)+1;
        timeval(ltsf:ltsf+yy)=timecols(mantimes(i):mantimes(i+1)-1);
    end
end
wvnr=datavar(2:f,1);
l=length(wvnr);
%Performs bounded nonlinear minimization using the medium scale trust
%region method.  For large scale method, one would need the gradient.
plot(wvnr,datavar(2:f,mantimes));
r=input('How many distinct peaks? ');
guessf=input('Estimate frequencies of those peaks: ')';
if (h=='y')|(h=='Y'),
    disp('When entering peak parameters and one or more of those');
    disp('  distinct peaks cannot be distinguished from the noise,
enter');
    disp('  the position as guessed above and the amplitude as zero.');
```

```
end
options=optimset('Display','notify','LargeScale','off','MaxFunEvals',1e
10,'MaxIter',1e10);
for i=1:noman,
    ok='n';
    while (ok=='n')|(ok=='N'),
        pok='n';
        while (pok=='n')|(pok=='N'),
            clear method;
            str=int2str(mantimesz(i));
            disp(['Perform manual fit of timeslice: ',str,'ps']);
            plot(wvnr,datavar(2:f,mantimes(i)));
            Iniparams=zeros(r,5);
            LB=zeros(r,5);
            UB=zeros(r,5);
            BRad=zeros(r,5);
            haveinip=input('Do you have the initial parameters saved as
a file? [{y}/n] ','s');
            if isempty(haveinip),
                haveinip='y';
            end
            if (haveinip=='y')|(haveinip=='Y'),
                if (h=='y')|(h=='Y'),
                    disp('Initial parameter file can be a 3rd-order
tensor,');
                    disp('  with page order: Guess, Lower bound, Upper
bound.');
                    disp('But this program can adapt to most reasonable
parameter');
                    disp('  file styles.');
                end
                inipfile=input('Name of initial parameters file:
','s');
                Inips=importdata(inipfile);
                [ir ic ip]=size(Inips);
                if (ir==r)&(ic==5)&(ip==2),
                    disp('You have entered a file with symmetric
bounds.');
                    Iniparams=Inips(:,:,1);
                    LB=Inips(:,:,1)-Inips(:,:,2);
                    UB=Inips(:,:,1)+Inips(:,:,2);
                elseif (ir==r)&(ic==5)&(ip==3),
                    disp('You have entered a file with asymmetric
bounds.');
                    Iniparams=Inips(:,:,1);
                    LB=Inips(:,:,2);
                    UB=Inips(:,:,3);
                elseif (ir==(2*r))&(ic==5)&(ip==1),
                    disp('You have entered a file with symmetric
bounds.');
                    Iniparams=Inips(1:r,:);
                    LB=Inips(1:r,:)-Inips((r+1):(2*r),:);
                    UB=Inips(1:r,:)+Inips((r+1):(2*r),:);
                elseif (ir==(3*r))&(ic==5)&(ip==1),
                    disp('You have entered a file with asymmetric
bounds.');
```

```
                    Iniparams=Inips(1:r,:);
                    LB=Inips((r+1):(2*r),:);
                    UB=Inips((2*r+1):(3*r),:);
                elseif (ir==r)&(ic==10)&(ip==1),
                    disp('You have entered a file with symmetric
bounds.');
                    disp('Assuming parameters are entered as
follows:');
                    disp('[Position,Position radius,Amplitude,Amp
radius, &c.]');
                    odds=[1,3,5,7,9];
                    evens=[2,4,6,8,10];
                    Iniparams=Inips(:,odds);
                    LB=Inips(:,odds)-Inips(:,evens);
                    UB=Inips(:,odds)+Inips(:,evens);
                elseif (ir==r)&(ic==15)&(ip==1),
                    disp('You have entered a file with asymmetric
bounds.');
                    disp('Assuming parameters are entered as
follows:');
                    disp('[Position,Pos LB,Pos UB,Amplitude,Amp LB, Amp
UB, %c.]');
                    guesscols=[1,4,7,10,13];
                    LBcols=[2,5,8,11,14];
                    UBcols=[3,6,9,12,15];
                    Iniparams=Inips(:,guesscols);
                    LB=Inips(:,LBcols);
                    UB=Inips(:,UBcols);
                else
                    disp('There is a problem with the parameter
file.');
                    disp('Generating initial parameters...');
                    RO=ones(r,1);
                    Iniparams=[guessf',10*RO,10*RO,zeros(r,1),RO];
                    LB=[1750*RO,-1000*RO,0.1*RO,zeros(r,2)];
                    UB=[2150*RO,1000*RO,50*RO,zeros(r,1),10*RO];
                end

plot(wvnr,datavar(2:f,mantimes(i)),wvnr,jvoigts(Iniparams(1:r,:),wvnr))
;
            else
                method=input('Are the constraints symmetric about the
initial guess parameters? [{y}/n] ','s');
                if (method=='n')|(method=='N')
                    disp('Enter the peak parameters as [Initial guess,
lower bound, upper bound]');
                    for j=1:r,
                        clear vert vrat;
                        pkno=int2str(guessf(j));
                        disp(['Enter following parameters for the peak
near ',pkno]);
                        pos(j,1:3)=input('Peak position (cm^{-1}) ');
                        amp(j,1:3)=input('Amplitude ');
                        wid(j,1:3)=input('Width ');
                        vert=input('Vertical offset {0,0,0} ');
                        if length(vert)==3,
```

```
                            ver(j,1:3)=vert;
                        else
                            ver(j,1:3)=[0,0,0];
                        end
                        vrat=input('Voigt ratio {1,0,10} ');
                        if length(vrat)==3,
                            rat(j,1:3)=vrat;
                        else
                            rat(j,1:3)=[1,0,10];
                        end

Iniparams(j,1:5)=[pos(j,1),amp(j,1),wid(j,1),ver(j,1),rat(j,1)];

LB(j,1:5)=[pos(j,2),amp(j,2),wid(j,2),ver(j,2),rat(j,2)];

UB(j,1:5)=[pos(j,3),amp(j,3),wid(j,3),ver(j,3),rat(j,3)];

plot(wvnr,datavar(2:f,mantimes(i)),wvnr,jvoigt(Iniparams(j,:),wvnr),wvn
r,jvoigts(Iniparams(1:j,:),wvnr));
                    end
                else
                    disp('Enter the peak parameters as [Initial guess,
bound radius]');
                    for j=1:r,
                        clear vert vrat;
                        pkno=int2str(guessf(j));
                        disp(['Enter following parameters for the peak
near ',pkno]);
                        pos(j,1:2)=input('Peak position (cm^{-1}) ');
                        amp(j,1:2)=input('Amplitude ');
                        wid(j,1:2)=input('Width ');
                        vert=input('Vertical offset {0,0} ');
                        if length(vert)==2,
                            ver(j,1:2)=vert;
                        else
                            ver(j,1:2)=[0,0];
                        end
                        vrat=input('Voigt ratio {1,1} ');
                        if length(vrat)==2,
                            rat(j,1:2)=vrat;
                        else
                            rat(j,1:2)=[1,(1-1E-6)];
                        end

Iniparams(j,1:5)=[pos(j,1),amp(j,1),wid(j,1),ver(j,1),rat(j,1)];

BRad(j,1:5)=[pos(j,2),amp(j,2),wid(j,2),ver(j,2),rat(j,2)];
                        LB=Iniparams-BRad;
                        UB=Iniparams+BRad;

plot(wvnr,datavar(2:f,mantimes(i)),wvnr,jvoigt(Iniparams(j,:),wvnr),wvn
r,jvoigts(Iniparams(1:j,:),wvnr));
                    end
                end
            end
```

```
            pok=input('Satisfied with the initial parameters? [{y}/n]
','s');
        end

Finparams=fmincon(@lswjvoigts,Iniparams,[],[],[],[],LB,UB,[],options,wv
nr,datavar(2:f,mantimes(i)),SDvar(2:f,mantimes(i)));

plot(wvnr,datavar(2:f,mantimes(i)),wvnr,jvoigts(Finparams,wvnr));
        deltachi=2;
        chi=sum(((datavar(2:f,mantimes(i))-
jvoigts(Finparams,wvnr))./(SDvar(2:f,mantimes(i)))).^2);
        count=1;
        while deltachi > (0.001*chi),
            chi=sum(((datavar(2:f,mantimes(i))-
jvoigts(Finparams,wvnr))./(SDvar(2:f,mantimes(i)))).^2);

Finparams=fmincon(@lswjvoigts,Finparams,[],[],[],[],LB,UB,[],options,wv
nr,datavar(2:f,mantimes(i)),SDvar(2:f,mantimes(i)));
            chin=sum(((datavar(2:f,mantimes(i))-
jvoigts(Finparams,wvnr))./(SDvar(2:f,mantimes(i)))).^2);

plot(wvnr,datavar(2:f,mantimes(i)),wvnr,jvoigts(Finparams,wvnr));
            count=count+1;
            deltachi=chi-chin
        end
        disp(count);

plot(wvnr,datavar(2:f,mantimes(i)),wvnr,jvoigts(Finparams,wvnr),wvnr,(d
atavar(2:f,mantimes(i))-jvoigts(Finparams,wvnr)));
        legend('Data','Fitted curve','Difference');
        disp('The parameters of the fitted curves are:');
        disp(Finparams);
        ok=input('Satisfied with the fit? [{y}/n] ','s');
    end
    if (ok=='n')|(ok=='N'),
        deltar=input('Change in number of peaks: ');
        r=r+deltar;
        if deltar~=0
            disp(guessf);
            guessf=input('Estimate frequencies of those peaks: ');
        end
    end
%Inputs final parameters into master tensor
    AllParams(:,:,mantimes(i))=Finparams;
end
%Fits remainder of times using an interpolation scheme.
%Boundaries are the extremes of the manfit times +/- a percentage.
for i=1:(noman-1),
    for j=1:r,
        port(j,:)=[0.001,0.2,0.1,0.1,0.1];
    end
    early=AllParams(:,:,mantimes(i));
    last=AllParams(:,:,mantimes(i+1));
    LBa=min(early,last);
    LB=LBa-abs(port.*LBa);
    UBa=max(early,last);
```

```
    UB=UBa+abs(port.*UBa);
    for j=1:(times(i,1)),
        Latest=AllParams(:,:,times(i,j+1)-1);
        Iniparams=0.5.*(early*(1-
j/(times(i,1)))+last*(j/(times(i,1))))+0.5.*Latest;
%Adjust bounds if latest fit goes beyond 'early' or 'last'
        if Latest<LBa,
            LB=min(LB,Latest);
            LB=LB-abs(port.*LB);
            disp('Adjusting lower bounds.');
        end
        if Latest>UBa,
            UB=min(UB,Latest);
            UB=UB-abs(port.*UB);
            disp('Adjusting upper bounds.');
        end

Finparams=fmincon(@lswjvoigts,Iniparams,[],[],[],[],LB,UB,[],options,wv
nr,datavar(2:f,times(i,j+1)),SDvar(2:f,times(i,j+1)));
        deltachi=5;
        chi=sum(((datavar(2:f,times(i,j+1))-
jvoigts(Finparams,wvnr))./(SDvar(2:f,times(i,j+1)))).^2);
        while deltachi > (0.001*chi),
            chi=sum(((datavar(2:f,times(i,j+1))-
jvoigts(Finparams,wvnr))./(SDvar(2:f,times(i,j+1)))).^2);

Finparams=fmincon(@lswjvoigts,Finparams,[],[],[],[],LB,UB,[],options,wv
nr,datavar(2:f,times(i,j+1)),SDvar(2:f,times(i,j+1)));
            chin=sum(((datavar(2:f,times(i,j+1))-
jvoigts(Finparams,wvnr))./(SDvar(2:f,times(i,j+1)))).^2);
            deltachi=chi-chin
        end

plot(wvnr,datavar(2:f,times(i,j+1)),wvnr,jvoigts(Finparams,wvnr));
        AllParams(:,:,times(i,j+1))=Finparams;
        for k=1:r,
            if abs(AllParams(k,2,times(i,j+1)))<0.05,
                AllParams(k,2,times(i,j+1))=0;
            end
        end
    end
end
%Computes areas of peaks at each time within 'range' wavenumbers of the
%center.
if (h=='y')|(h=='Y'),
    disp('Omnivoigt will now compute the area of each peak.');
end
range=input('Compute area to within how many wavenumbers? {50} ');
if isempty(range),
    range=50;
end
[p q x]=size(AllParams);
areas=zeros(p,r);
for i=1:r,
    for j=mantimes(1):mantimes(noman),
        AreaParams=[AllParams(i,1:3,j),0,AllParams(i,5,j)];
```

```
        if AreaParams(2)==0,
            areas(i,j)=0;
        else
            areas(i,j)=quad(@jvoigtb,AreaParams(1)-
range,AreaParams(1)+range,1E-6,0,AreaParams);
        end
    end
end
%Prepares arrays of peak positions and of fitted timeslices; queries
%user whether to plot peak positions and peak areas.
tts=length(timeval);
posits(1:r,1:tts)=AllParams(1:r,1,mantimes(1):mantimes(noman));
for i=1:r,
    lgnd{i}=sprintf('Peak %d',i);
end
plotp=input('Do you wish to plot the peak positions versus time?
[y/{n}] ','s');
if (plotp=='y')|(plotp=='Y'),
    plot(timeval,posits);
    xlabel('Time (ps)');
    ylabel('Peak Position (cm^{-1})');
    legend(lgnd);
end
plota=input('Do you wish to plot the peak areas versus time? [y/{n}]
','s');
if (plota=='y')|(plota=='Y'),
    figure;
    plot(timeval,areas(1:r,mantimes(1):mantimes(noman)));
    xlabel('Time (ps)');
    ylabel('Peak Area');
    legend(lgnd);
end
%Saves parameters and areas
outname=input('Name your data: ','s');
save(strcat(outname,'_vparams.dat'),'AllParams');
save(strcat(outname,'_vareas.dat'),'areas');
%Important variable glossary:
%   AllParams   3rd-order tensor where (rows->peaks),(columns->peak
%               params),(pages->times)
%   areas       matrix where (rows->peaks),(columns->times)
%   BRad        bound radius
%   datavar     matrix of data where top row is times and first column
%               is wavenumbers
%   early       earliest manfit timeslice of a region
%   haveinip    tensor of initial guess parameters
%   timeval     array of all times fitted
%   Iniparams   input parameters for fitting a time
%   last        last manfit timeslice of a region
%   Latest      timeslice fit prior to current timeslice
%   LB          lower bound
%   LBa         lower bound prior to extension by 'port'
%   mantimes    array of all times to manually fit
%   noman       number of manually fit times
%   port        percentages of UB,LB to increase bound region
%   r           number of peaks
%   SDvar       matrix of standard deviations corresponding to
```

```
%               'datavar'
%   times       matrix whose number of rows are number of autofit
%               regions,whose first column is number of times to
%               autofit in that region, whose other columns are the
%               timeslice columns in
%               that region
%   UB          upper bound
%   UBa         upper bound prior to extension by 'port'
```

jvoigt.m

```
function v=jvoigt(a,X)
%Voigt function where the parameters are:
%   a(1)    peak position
%   a(2)    amplitude
%   a(3)    width
%   a(4)    vertical offset
%   a(5)    ratio of Lorentz to Doppler widths
v=a(2)*voigt((X-a(1))*2/(a(3)),a(5)/sqrt(log(2)))+a(4);
```

jvoigts.m

```
function f=jvoigts(a,X)
%Multiple-Voigt function where the parameters are:
%   a(i,1)    peak position
%   a(i,2)    amplitude
%   a(i,3)    width
%   a(i,4)    vertical offset
%   a(i,5)    ratio of Lorentz to Doppler widths
%Quantity-adaptive
[r c]=size(a);
m=zeros(length(X),r);
for i=1:r,
    m(:,i)=jvoigt(a(i,:),X);
end
f=sum(m,2);
```

jvoigtb.m

```
function v=jvoigtb(X,a)
%Voigt function where the parameters are:
%   a(1)    peak position
%   a(2)    amplitude
%   a(3)    width
%   a(4)    vertical offset
%   a(5)    ratio of Lorentz to Doppler widths
v=a(2)*voigt((X-a(1))*2/(a(3)),a(5)/sqrt(log(2)))+a(4);
```

lswjvoigts.m

```
function f=lswjvoigts(a,X,Y,s)
%Used for weighted, least-squares minimization of multiple voigts
f1=jvoigts(a,X);
f=sum(((Y-f1)./s).^2);
```